12-2012

Validation of Weak Form Thermal Analysis Algorithms Supporting Thermal Signature Generation

Elton Lewis Freeman
efreema4@utk.edu

To the Graduate Council:

I am submitting herewith a thesis written by Elton Lewis Freeman entitled "Validation of Weak Form Thermal Analysis Algorithms Supporting Thermal Signature Generation." I have examined the final electronic copy of this thesis for form and content and recommend that it be accepted in partial fulfillment of the requirements for the degree of Master of Science, with a major in Engineering Science.

Allen Jerome Baker, Major Professor

We have read this thesis and recommend its acceptance:

Kwai Lam Wong, Jay I. Frankel

Accepted for the Council:
Carolyn R. Hodges

Vice Provost and Dean of the Graduate School

(Original signatures are on file with official student records.)

Validation of Weak Form Thermal Analysis Algorithms Supporting Thermal Signature Generation

A Thesis Presented for

The Master of Science

Degree

The University of Tennessee, Knoxville

Elton Lewis Freeman

December 2012

Dedication

I would like to dedicate this to my granddad Leonard (90 years), who got me started when I was young to be an engineer.

Acknowledgments

I would like to thank my advisor, Dr. A.J.Baker for his theoretical expertise in this subject matter. I would also like to thank Joe Orzechowski for his expertise in aPSE (a Problem Solving Environment), his FORTRAN code, over the past 40 years of refinements and improvements, which will be inherited to my hands as continuation of future computational sciences in, a new age of computing. I would like thank Dr. Kwai Lam Wong for his expertise in computational understanding with theory implementation and challenges in parallel computing environments.

I would like to thank the US Department of Defense, US Army contract W91ZLK-10-0007 for funding for this project.

I am thankful for Dr. Jeff Sander's help with these meteorological data and the Bobcat Salmon data files. The name Bobcat Salmon has a unique story as Jeff was confronted with constructing an experimental apparatus to measure meteorological data for on thermal energy budgets for two flat black plates. When asked what to name his experiment, he then remembered what his cat Bob had eaten the night before, "Salmon", hence the name of the experimental data file supporting validations detailed in this thesis.

Quotes

Over the period of conducting my research and writing this thesis, some really simple qoutes that have a well defined meaning are:

"Whether at work or at play, do your best"
Green Hall,Berry College, Rome Ga 30161

"... who needs reverse, life moves forward"
Dr. A.J Baker

"When there is a fork in the road take it, I did and ended up here"
Dr. A.J.Baker

"Does it work?"
Dr. Kwai Lam Wong

Abstract

Extremization of a weak form for the continuum energy conservation principle differential equation naturally implements fluid convection and radiation as flux Robin boundary conditions associated with unsteady heat transfer. Combining a spatial semi-discretization via finite element trial space basis functions with time-accurate integration generates a totally node-based algebraic statement for computing. Closure for gray body radiation is a newly derived node-based radiosity formulation generating piecewise discontinuous solutions, while that for natural-forced-mixed convection heat transfer is extracted from the literature. Algorithm performance, mathematically predicted by asymptotic convergence theory, is subsequently validated with data obtained in 24 hour diurnal field experiments for distinct thickness flat plates and a cube-shaped three dimensional object.

Contents

List of Tables

List of Figures

Nomenclature

α	Absorptivity of incoming radiation.
β	Series of trial functions, guess to exact solution.
β_{air}	Thermal expansion coefficient of air, $\left[\frac{1}{K}\right]$.
$\cap$	Non overlapping sum of elements.
Δt	Time step, $[seconds]$.
δ	Transmission incoming radiation.
ϵ	Emissivity, a material property.
η_{air}	Natural convection switch.
η_{conv}	Convection switch term.
γ	Energy norm computing parameter.
k	Italic, linear basis order , 1,2,3,...
$[ONE]$	Matrix composed on 1's.
$\|\mathbf{A}\|$	Magnitude earth sun distance, used in solar code, normalized to 149.6010^9 m.
$\|T\|_E$	Energy norm for temperature, $[K]$.

$\mathcal{L}(\phi)$	Partial differential equation (P.D.E) for mass conservation.
$\mathcal{L}(T)$	Partial differential equation (P.D.E) for energy.
ν	Kinematic viscosity of air, $\left[\frac{m^2}{s}\right]$.
Ω	Domain of influence, solution domain.
ϕ	Potential function for velocity.
Φ_φ	Test function.
ϕ_i	Angle to surface k's unit normal, radiation reveived from surface k.
ϕ_k	Angle to surface k's unit normal, radiation emitted to surface i.
Ψ_β	Trial function.
$\Re^n$	An n dimensional Euclidean space.
ρ	Density, general examples, no subscripts, $\left[\frac{kg}{m^3}\right]$.
ρ_{air}	Density of air, $\left[\frac{kg}{m^3}\right]$.
ρ_{al}	Density of aluminum, $\left[\frac{kg}{m^3}\right]$.
ρ_i	Reflectivity of the ith surface facet.
ρ_{st}	Density of steel, $\left[\frac{kg}{m^3}\right]$.
σ	Stefan Boltzmann's constant, 5.67x^{10} $\left[\frac{W}{m^2K^4}\right]$.
η	Coordinate global space transformation.
$\mathbf{CG3}_{dn}$	Ground radiation, allways upwelling, $\left[\frac{W}{m^2}\right]$.
$\mathbf{CG3}_{up}$	Sky diffuse radiation, allways downwelling $\left[\frac{W}{m^2}\right]$.

$\mathbf{CM3}_{\boldsymbol{dn}}$	Reflected solar radiation, allways upwelling $\left[\frac{W}{m^2}\right]$.
$\mathbf{CM3}_{\boldsymbol{up}}$	Direct solar radiation, $\left[\frac{W}{m^2}\right]$.
$\mathbf{f}(\mathrm{t})$	Boundary terms appearing in PDE.
$\mathbf{i}$, $\mathbf{j}$, $\mathbf{k}$	Cartesian unit vectors.
PYRO	Diffuse solar radiation, allways downwelling $\left[\frac{W}{m^2}\right]$.
$\mathbf{RAD}_{\boldsymbol{net}}$	Net radiation, $\left[\frac{W}{m^2}\right]$.
$\mathbf{v}(t)$	Sun's position vector, time dependent.
θTS	Theta series time stepping.
θ	Theta implicitness, θ=0 Explicit, θ=1 Implicit, θ=0.5 Semi-implicit.
φ	Series of test functions appearing in approximation of solution.
$l(\phi)$	Robin boundary terms appearing in Laplacian P.D.E.
$l(T)$	Robin boundary terms appearing in energy P.D.E.
aPSE	a Problem Solving Environment, code development.
C_1	Forced convection coefficient.
C_2	Forced convection coefficient.
C_3	Forced convection coefficient.
$\mathrm{c}_{p,air}$	Specific heat capacity air, $\left[\frac{kJ}{kgK}\right]$.
$\mathrm{c}_{p,al}$	Specific heat capacity aluminum, $\left[\frac{kJ}{kgK}\right]$.
$\mathrm{c}_{p,st}$	Specific heat capacity steel, $\left[\frac{kJ}{kgK}\right]$.

c_p	Specific heat capacity, general examples, $\left[\frac{kJ}{kgK}\right]$.
ConvB	Pre-computed bottom convection coefficient, in figues $\left[\frac{W}{m^2K}\right]$.
ConvT	Pre-computed top convection coefficient, in figures $\left[\frac{W}{m^2K}\right]$.
$d\Omega$	Differential volume, $[m^3]$.
$d\sigma$	Differential surface area, $[m^2]$.
$\det_e$	Measure of the area of the element, $[m^2]$.
diag($\bullet$)	Diagonal square matrix.
EXPT	Experimental temperature data measurements, validation, $[K]$.
f(Θ)	Approximating error in computing energy norm.
F_{ki}	View factor or shape factor.
g	Gravitational constant, $9.80\left[\frac{m}{s^2}\right]$.
$G_{k,i}$	Gebhart factor, fraction of energy that leaves surface k and absorbed by surface i.
GWS^h	Weak statement for discretized solution domain.
GWS^N	Weak statment using the approximated guess.
h	Spatial mesh refinement parameter, no subscripts.
H_0	Norm used in computing radiosity.
h_{conv}	Convection coefficient, mixed, $\left[\frac{W}{m^2K}\right]$.
h_{for}	Convection coefficient, forced convection, $\left[\frac{W}{m^2K}\right]$.
h_{nat}	Convection coefficient, natural convection, $\left[\frac{W}{m^2K}\right]$.

k	Thermal conductivity, used as a general placeholder, $\left[\frac{W}{mK}\right]$.
k_{air}	Thermal conductivity, air, $\left[\frac{W}{mK}\right]$.
k_{al}	Thermal conductivity, aluminum, $\left[\frac{W}{mK}\right]$.
K_{ki}	Symmetric kernel, used in Fredholm integrals.
k_{st}	Thermal conductivity, steel, $\left[\frac{W}{mK}\right]$.
L_c	Characteristic length scale, $[m]$.
M	Mesh measure, total number of elements.
n	Exponent on non-dimensional groups, Gr and Pr.
$q^{'}$	Thermal energy flux, flows opposite to gradient of temperature.
RES	Residual, $[K]$.
SRC	also given as s, volume energy source, generation term, $\left[\frac{W}{m^3}\right]$.
T	Solution variable, energy conservation, $[K]$.
$T_{\beta}(t)$	Basis function, expansion coefficient.
T_{amb}	Ambient air temperature, meteorological data input, $[K]$.
t_{n+1}	Future time, $[seconds]$.
t_n	Current time, $[seconds]$.
T_{rad}	Temperature of participating medium, $[K]$.
T_{ref}	Farfield background temperature T_{ground} and/or T_{sky}, $[K]$.
VAWS	Vector averaged wind speed, meteorological data input, $\left[\frac{m}{s}\right]$.
x	Characteristic length scale appearing in Reynolds number, $[m]$.

Chapter 1

Introduction

1.1 A Need for an Improved Heat Transfer Algorithm

Heat transfer is classified into various mechanisms, such as thermal conduction, thermal convection, thermal radiation, and transfer of energy by phase changes. This thesis explores the first three mechanisms for applications in thermal imagery. For example, the Department of Defense (DoD) uses thermal imagery to track and monitor threat assessment. Ground targets generate characteristic emissions in the optical bands that are inadvertent to their propulsion and vital to the detection process. The most prominent of these are associated with the combustion of fuel during boost and sustain phases.

The automotive community has adopted visual inspection and maintenance of operating components in a vehicle with the help of thermal images that represent the heat pattern of the components under consideration. Thermal images of automotive components taken over a period of time can be analyzed and inspected for certain abnormalities. Changes in the form, material or location of the automotive parts

result in the expense of time and physical work. Simulation of thermal images of automotive parts in a virtual environment can be done for various applications ranging from fluid flow analysis to complex thermal management of components.

Conjugate heat transfer algorithms can simulate complex geometries such as ground targets or automotive components. The problem posed, the exact solution T($\mathbf{x}$,t) can never be found analytically! Numerical errors accumulate from (1) round off (2) truncation (3) human interaction and (4) approximation errors. Human error can be eradicated, but truncation and round off errors are inherited. The approximation errors can be minimized with the aid of weak formulations (wf), and their underlying theory hence the scope of this thesis.

A test to generate validation data was carried out at the Redstone Arsenal in Huntsville, Alabama. These tests were conducted on several targets, of which the simplest targets were horizontal plates of two thicknesses exposed to typical spring meteorological conditions. A $\frac{1}{8}$ inch and 1 inch thickness aluminum plates were placed on wooden pegs about 1 foot off the ground, Figure 1.1. Targets can be composed of several or more flat surfaces; therefore the horizontal plate serves as the base test for a proposed conjugate heat transfer algorithm. As seen in Figure 1.2 the Bobcat Salmon flat plate simulation is still applicable to the top of Cubi like figure.

A second test case, Cubi uses potential flow practice to generate an immersed flow field. Assumptions include a flow that is frictionless irrotational and laminar. Even though all real fluids are viscous to some degree, if the effects of viscosity is sufficiently small then the accompanying frictional effects may be negligible. Potential flow practice assumes boundary layers as nonexistent, and the fluid flow replicates the contours of the solid surface convection correlations are with freestream velocity

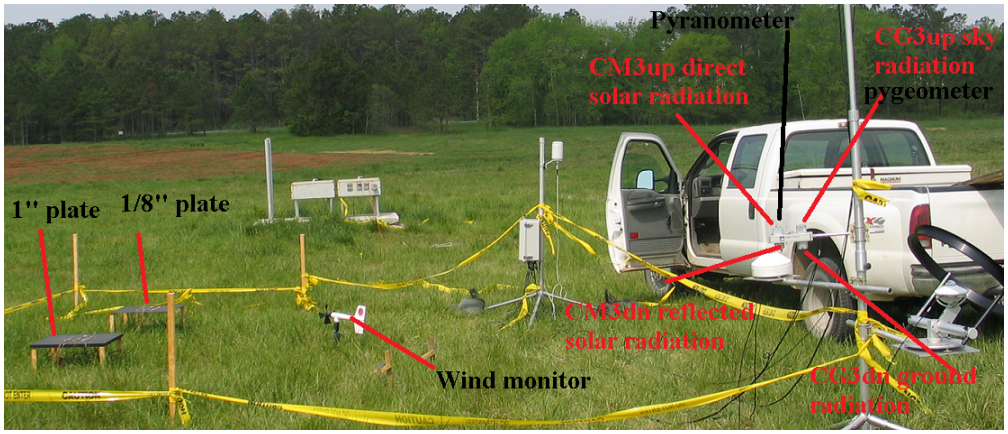

Figure 1.1: Experimental apparatus used at meteorological station for 04-2006.

U_∞. Figure (1.2) details perspectives of Bobcat Salmon experiment Cubi object, and Cubi L-shape facing due north showing early morning residual condensation.

1.2 Meteorological Measurements

The atmosphere, a gaseous envelope surrounding the earth, is held by gravity and has maximum density just above the earth's surface. This atmosphere becomes less dense with increasing distance from the ground, to becoming hardly indistinguishable from the interplanetary gas. Therefore, there is not an upper limit "top" of the atmosphere. An important, but often difficult measurement is long wave radiation balance. The atmosphere is transparent to long wave radiation, and peculiar only to a bandwidth spectral range of 8 to 14 μm which is called the *atmospheric window*.

Within this spectral range, the earth is able to maintain an equilibrium temperature by emitting heat gained from absorption from the sun. The sun can be approximated as a blackbody, with an equivalent radiation temperature of 5,700 K, of which 99%

Figure 1.2: Perspective of Cubi, facing due north.

of its energy is contained less than wavelengths of 4 μm is considered as *short wave*. The equivalent radiant temperature of the earth's surface is about 275 K.

Downward long wave radiation that reaches the earth is a result of atmospheric reemission. Reemission is the reversible effect of absorption of short wave radiation by chemical elements, for example, water, oxygen, ozone, carbon dioxide, etc. These elements readmit radiation back to the earth's surface as short wave radiation.

The remaining unabsorbed portion of the earth's radiation then escapes into space. Under clear skies and object can be cooled below ambient air temperature by radiative heat loss to the sky. This may also explain why in some cases frost will form on the upward side of an object as oppossed to its side.

The net radiant energy available at the earth's surface derives from the difference in several upward and downward directed radiation currents. The spectral range being roughly 0.3 to 50 μm, which covers both solar radiation, 0.3 to 3 μm, and the far infrared radiation, 5 to 50 μm. The net radiation applies to a black, homogeneous

Figure 1.3: Components of the CNR1. Pyranometer (left) and pygeometer (right).

plate in Figure 1.4 as well as to the Cubi. Figure 1.1 details a scene from the meteorological station, the experimental apparatus measuring data supporting a heat transfer algorithm. The two thickness plates are in proximity, to the wind monitor, pyranometer, and pyrgeometer. Pyranometers are used to measure solar irradiance on a planar surface and is a sensor that is designed to measure the solar radiation flux density $\frac{W}{m^2}$ from a field of view of 180^o degrees. Pyrgeometers are designed to measure the atmospherically and ground infrared radiation. A 4-component net-radiometer measures 4 separate components of the surface radiation balance Figure 1.3. Direct solar radiation ($\mathbf{CM3}_{up}$), reflected solar radiation ($\mathbf{CM3}_{dn}$), infrared sky radiation ($\mathbf{CG3}_{up}$), and infrared ground radiation ($\mathbf{CG3}_{dn}$). Table 1.1 details data from pyranometer and pyrgeometer sensors along with symbol and spectral range.

Other sensory data needed for validation include an ambient temperature sensor used to measure T_{amb} and wind monitor Figure 1.5 used for measuring vector averaged wind speed (VAWS). Ambient sensor resolution ~ 0.1 K with a frequency of 5 minutes.

Table 1.1: Solar measurements from meteorological station.

$\mathbf{CM3_{up}}$	Direct solar radiation (short wave)	[0.305-2.800 μm]
$\mathbf{CM3_{dn}}$	Reflected solar radiation (long wave)	[0.305-2.800 μm]
CG3up	Sky radiation (long wave)	[5.00 - 42.00 μm]
CG3dn	Ground radiation (long wave)	[5.00 - 42.00 μm]
$\mathbf{RAD_{net}}$	Net radiation	[5.00 - 42.00 μm]
PYRO	Specular solar radiation	[5.00 - 42.00 μm]
T_{grnd}	Derived soil temperature	$\sim \frac{\sigma}{CG3_{dn}}$
T_{sky}	Derived sky temperature	$\sim \frac{\sigma}{CG3_{up}}$

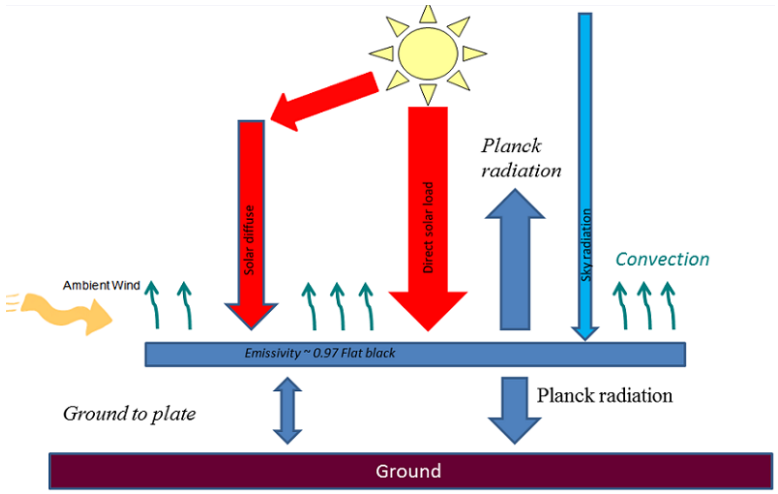

Figure 1.4: The Bobcat Salmon energy budget.

A wind monitor (Young 05103), measures wind speed with a resolution of 0.1 $\frac{m}{s}$ and pivots to measure wind velocity over a 360^o degree angle. A typical wind measurement and velocity datum given in Figure 1.6, shows the wind direction, which is mostly North West, and the bottom-bottom of the figure showing the wind magnitude. Over a typical day, the wind speed can change due to thermal affects, such as atmospheric *turn over*. These data are critical for determination of the thermal energy dissipated by convection.

The cold sky can act as a heat sink for radiating bodies. The sky temperature is lower than the ambient air temperature because the atmoshpheric temperature

Figure 1.5: The Young's wind monitor measures vector averaged windspeed.

decreases with increasing elevation. The emissivity of sky has been measured by [1] as a linear function Eq. (1.1)

$$e_{sky} \sim 0.7223 + 0.006349 T_{dp} \tag{1.1}$$

1.3 Measured Solution Data by Thermocouples

A Problem Solving Environment (aPSE-FORTRAN driver) uses heat transfer subroutines to compute the energy budget across Bobcat Salmon. The simulation output will be compared against measured data from one of four thermocouples. Temperature data include the plate upper surface centroid, recorded by a built-back thermocouple (TC), two surface-attached TCs adjacent to the plate centroid, Figure 1.7. Surface mount thermocouples are exposed to the surrounding environment, and they often need to be isolated. Sunshine, air flow, and nearby heat sources can significantly affect these measurements. The epoxy resin *must* couple as well as protect the thermocouple from corrosion. We have decided to compare simulated results to those of built-back

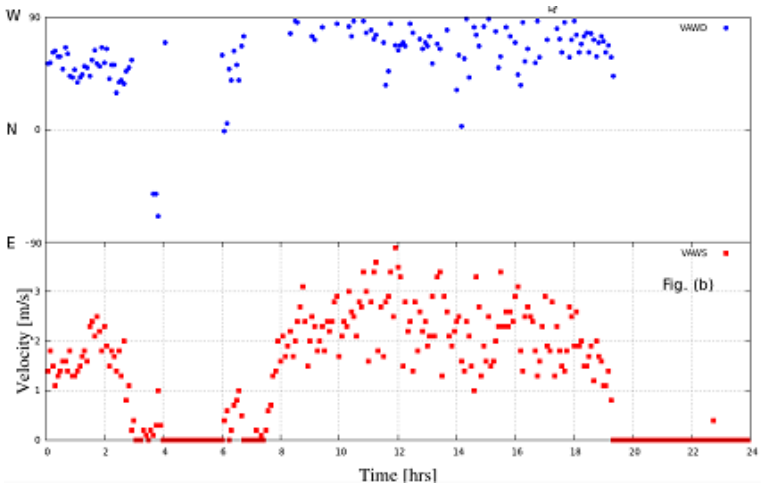

Figure 1.6: Wind data with direction and magnituded.

thermocouples due to shielding of environmental impacts, see Figure 1.8. The extreme deviation of surface-adhered TC from the accurate built and built-back TCs is ~ 2 Kelvin for 04-12-2006.

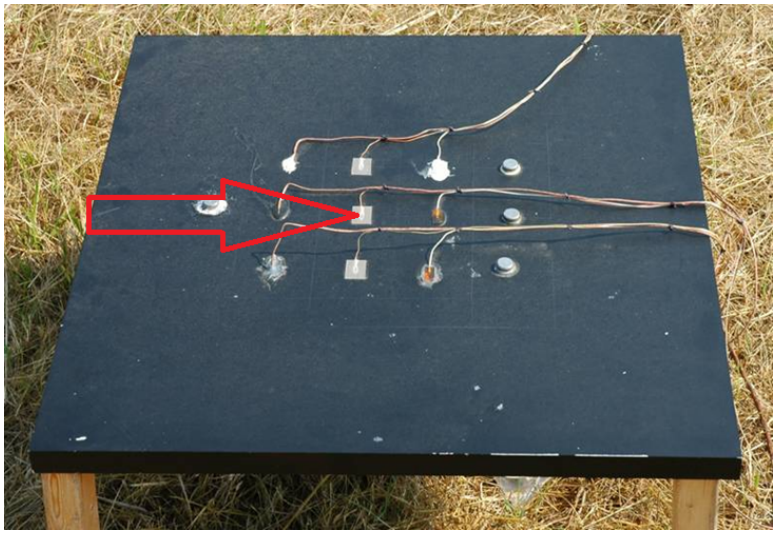

Figure 1.7: Cubi thermal sensors, from left; self-adhesive, built, built-back, and button (not used).

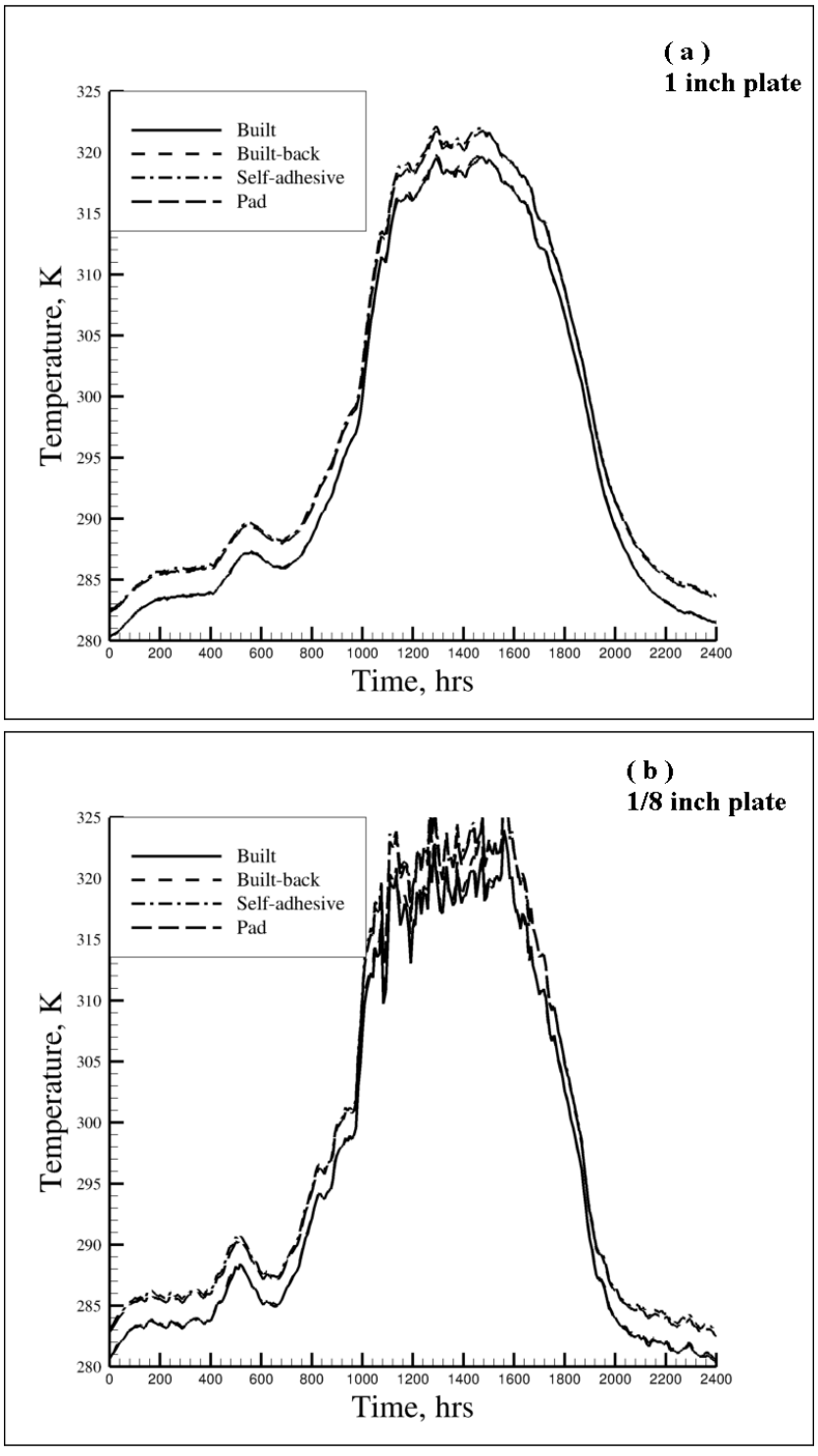

Figure 1.8: 4 temperature sensor performance profiles for 04-12-2012.

Chapter 2

Conservation Principles

2.1 The Science and Technology Demands

Rapid developments in computing power and anomaly detection algorithms have led to the possibility of real time target identification, location, and designation. The science and technology challenge is to incorporate a high level of signature model fidelity, a requirement to simulate a modern sensor in real-time in a hardware-in-the-loop (HWIL) simulation. With spectral data of sufficient resolution, it is possible to better distinguish, differentiate, classify, or recognize more subtle features in the imagery and also detect spatially unresolved features. The most important challenge in real-time simulation requires new approaches in the computational data generated by the simulation.

This research study was conducted under the US Department of Defense (STAR) prime contract W91ZLK-10-C-0007 entitled, "SCALABLE THERMAL ANALYSIS FOR REAL-TIME SIGNATURES (STAR)," to Trideum, Inc., with the University of Tennessee, CFD Laboratory coupled with the Joint Institute for Computational Science, the prime sub-contractor.

2.2 Energy

The continuum unsteady thermal energy conservation principle partial differential equation (PDE) appends the all-important radiation 4^{th} order nonlinear boundary condition (BC). Target immersion in an atmospheric (fluid) flow field adds thermal convection BCs, and all BCs are explicitly dependent on time. The n-dimensional time-dependent PDE + BCs statement for a domain of influence on $\Omega \subset \Re^n$

$$\mathcal{L}(\mathbf{x}, t, T) = \rho_{al} c_{p,al} \frac{\partial T}{\partial t} - \vec{\nabla} \bullet \left[k_{al} \left(\mathbf{x} \right) \vec{\nabla} T \right] - s \left(\mathbf{x}, t \right) = 0. \tag{2.1}$$

$$l\left(T\right) = k_{al} \vec{\nabla} T \bullet \mathbf{n} + h_{conv} \left(T - T_{atm} \right) + \sigma \epsilon \left(T^4 - T_{ref}^4 \right) + \mathbf{f}\left(t\right) \bullet \mathbf{n} = 0$$

The thermo-physical properties ρ_{al}, $c_{p,al}$ and k_{al} are density, specific heat and thermal conductivity of the target material (see Appendix; Tables (A.1, A.2)). The thermal conductivity of T-6063 Aluminum (al) is assumed uniform in space $k_{al}(\mathbf{x}) \sim k_{al}$. In the Robin BC h_{conv} is convective heat transfer coefficient for a velocity field with exchange temperature distribution T_{amb}, and radiation heat exchange is the Planck emission with a reference background temperature T_{ref} as T_{sky} or T_{grnd} or both. Finally, $\mathbf{f}(t)$ is an imposed heat flux vector, e.g., solar and far field diffuse radiation. The emissivity appearing is taken for Krylon Flat black paint $\epsilon \sim 0.97$.

The weak form theory *approximation* to the unavailable solution $T(\mathbf{x}, t)$ of Eq. (2.1) is the continuum expression Eq. (2.2)

$$T^N(\mathbf{x}, t) \equiv \sum_{\beta=1}^{N} \Phi_\beta(\mathbf{x}) T_\beta(t) \tag{2.2}$$

for $\Phi_\beta(\mathbf{x})$ the approximation *trial space*, a set of functions $1 \leq \beta \leq N$. Extremizing the *approximation error* $e^N(\mathbf{x}, t) \equiv T(\mathbf{x},t) - T^N(\mathbf{x}, t)$ accrues to enforcing the continuum Galerkin weak statement $\left(GWS^N\right)$. Substituting the approximation given in Eq.

(2.2) into Eq. (2.1) gives the measure of the error given as

$$L(T^N(\mathbf{x},t)) \neq 0$$

$$GWS^N \equiv \int_\Omega \Phi_\varphi(\mathbf{x}) L(T^N) d\tau \equiv 0 \tag{2.3}$$

Equation (2.3) uses an arbitrary choice of a weight functions, Φ_φ (or test functions) for $1 \leq \varphi \leq$ N. The Galerkin weak statement is optimal when, the weight function is chosen to be identical to the trial function ($\Phi_\varphi = \Psi_\beta$), hence minimizes the approximation error.

$$\begin{aligned} GWS^N \equiv & \int_\Omega \Psi_\beta \left(\rho_{al} c_{p,al} \frac{\partial T^N}{\partial t} - s \right) d\Omega + k_{al} \int_\Omega \vec{\nabla}\Psi_\beta \bullet \vec{\nabla} T^N d\Omega \\ & + \oint_{\partial\Omega_{conv} \cap \partial\Omega} \Psi_\beta \left[h_{conv} \left(T^N - T_{amb} \right) \right] d\sigma \\ & + \oint_{\partial\Omega_{flux} \cap \partial\Omega} \Psi_\beta \mathbf{f}(t) \bullet \ \mathbf{n} \ d\sigma - \oint_{\partial\Omega_{else} \cap \partial\Omega} \Psi_\beta k_{al} \vec{\nabla} T^N \bullet \ \mathbf{n} \ d\sigma \end{aligned} \tag{2.4}$$

Equation (2.4) was generated using Green's theorem. Green's theorem uses integration over volume and surface solution domain. The theorem relates the interrior flux $q' = -k \nabla T$ as well as a vector field through a surface $\mathbf{f}(t)$ to the behavior of the vector field inside the surface. Recall that thermal energy flows down a temperature gradient (-). The second integral in the terminal line of Eq. (2.4) enables heat flux prediction through portions of the domain boundary $\partial\Omega$ upon which Robin BCs are specified. For example a general example fo Green Gauss integeral,

omission of time

$$\begin{aligned}
&\int_{\Omega}\left(\vec{\nabla}\bullet\mathbf{q}^{'}\right)d\Omega=\oint_{\partial\Omega}\mathbf{f}(t)\bullet\mathbf{n}d\sigma\\
&\int_{\Omega}\left(\vec{\nabla}\bullet k\vec{\nabla}T\right)d\Omega=\oint_{\partial\Omega}\mathbf{f}(t)\bullet\mathbf{n}d\sigma\\
&GWS=k\int_{\Omega}\vec{\nabla}^{2}Td\Omega-\oint_{\partial\Omega}\mathbf{f}(t)\bullet\mathbf{n}d\sigma=0
\end{aligned}\tag{2.5}$$

Applying Green-Gauss Theorem, and recognizing that all interior generated surface integral vanish identically. Where $\partial\Omega$ is the boundary of Ω. The surface integral will be zero for any homogeneous Neumann boundary condition. These results are also given in [2] from Chapters 9,10.

Conceptually solving Eq.(2.4), the time derivative matrix $\frac{dT^{N}(t)}{dt}$ is the data necessary for a time Taylor series (TS) underlying *all* first order partial differential equation (ODE) integration algorithms. The semi-discretized finite element Temperature weak statements then forms the algebraic partial differential equations as in Eqs.(2.6),(2.7), also see [2] pp 185-188.

$$GWS^{h}\equiv[M]\frac{dT}{dt}+\{RES\{T\}\}\equiv\{0\}\tag{2.6}$$

The [M] matrix in Eqs. (2.6),(2.7) results from the integral multiplying $\mathrm{d}\frac{\{T(t)\}}{dt}$ in Eq. (2.4) *only*, while $\{RES(T)\}$ contains all remaining terms. A description and derivation of matrices used for computing was completed in a previous work and the reader is advised to persue [3]. pp. 277-280, for a description of all matrices used throughout this document. For iteration index p, the matrix solution process for Eq.

(2.1) is

$$
\begin{aligned}
GWS^N(t) + \theta TS \equiv & \{F(\{T(t)\})\} \\
\{F(\{T(t)\})\} = & [M](\{T\}_{n+1} - (\{T\}_n) \\
& + \Delta t \left[(\theta)\{RES(\{T\})\}_{n+1} + (1-\theta)\{RES(\{T\})\}_n\right] \\
& = \{0\}
\end{aligned}
\tag{2.7}
$$

A one step Euler scheme is used to integrate through the transient solution. In Eq. (2.7) n denotes the n^{th} time station, t_n current time, then $t_{n+1} = t_n + \Delta t$ and $\theta = 0.5$ represents the trapezoidal rule, while $\theta = 1$ represents the full implicit backward Euler integration scheme. Equation (2.7) is used to represents a non-linear system of partial differential equations that must be solved iteratively. The Newton-Raphson algorithm is used and the procedure is shown in Eq. (2.8). The first two lines details the procedure for updating the DOF and residual for iterate p = 1,2,3,4, ... until convergence n+1.

$$
\begin{aligned}
\{T\}^0_{n+1} = & \{T\}^0_n \\
\{F(\{T(t)\}\}^0_{n+1} = & \{F(\{T(t)\}\}^0_n \\
[JAC(\{T\})]\{\Delta T\}^{p+1} = & -\{F(\{T(t)\})\}^p_{n+1} \\
[JAC(\{T\})] = & \frac{\partial\{F(\{T\})\}}{\partial\{T\}} \\
\{T\}^{p+1}_{n+1} = & \{T\}^p_{n+1} + \{\Delta T\}^{p+1}_{n+1} = \{T\}^p_{n+1} + \sum_{\alpha=0}^{p}\{\Delta T\}^{\alpha+1}_{n+1}
\end{aligned}
\tag{2.8}
$$

The terminal line of Eq. (2.8) defines the solution vector at the (p+1) iteration, in terms of an incremental change $\{\Delta T\}^{p+1}$ more detail is also provided in [2],[9].

2.3 Weak form algorithm transition to computable form

The weak form theory now complete, Eq.(2.4) is implemented via replacement of the global span trial space with a finite element *trial space basis* $\Psi_\beta(\mathbf{x}), \{N_k(\bullet)\}$ from Chapter 5 of [2]. Efficiency accrues to defining the Lagrange *linear* ($k = 1$) basis spanning tetrahedron/ hexahedron domains Ω_e of a (finite element) discretization Ω^h of the domain Ω of PDE Eq. (2.1). The precise restatement of Eq. (2.2) for this *semi-discrete* construction is

$$\begin{gathered} T^N(\mathbf{x},t) \equiv \sum_{\beta=1}^{N} \Psi_\beta(\mathbf{x}) T_\beta(t) \Rightarrow T^h(\mathbf{x},t) \equiv \cup_e^M T_e(\mathbf{x},t) \\ T_e(\mathbf{x},t) \equiv \{N_1(\eta(\mathbf{x}))\}^T \{T(t)\}_e \end{gathered} \tag{2.9}$$

where $\cup_e^M$ denotes *union*, the non-overlapping sum of each element level approximation $\mathrm{T}_e(\mathbf{x},\mathrm{t})$, $1 < \mathrm{e} < \mathrm{M}$. The functional form $\{N_1(\eta(\mathbf{x}))\}$ emphasizes transformation from global $\mathbf{x}$ to element-intrinsic η coordinates on all M elements Ω_e of the spatial semi-discretization $\Omega^h = \cup_e^M \Omega_e$.

The GWS^N Eq. (2.4) is transformed to discrete GWS^h via Eq. (2.9). The elements constituting Ω^h will never span two distinct materials hence first divide Eq. (2.1) through by ρc_p. Then $\mathrm{k}/\rho\ \mathrm{c}_p \rightarrow \kappa_e$, the element thermal diffusivity, hence also $\rho c_p \rightarrow (\rho c_p)_e$, and discarding the terminal integral in Eq. (2.4) as non-essential, the weak

form operation $\mathrm{GWS}^N \equiv \int_\Omega \Psi\ (\mathbf{x})\ \mathrm{L}(\mathrm{T}^N)\ \mathrm{d}\ \tau \Rightarrow \mathrm{GWS}^h(\mathrm{T}^h)$

$$
\begin{aligned}
GWS^h = S_e^M & \left[\begin{array}{c} \{N_1\} \left(\frac{\partial T_e}{\partial t} - \frac{SRC}{\rho_{al} c_{p,al}} \right) d\tau \\ + \int_{\Omega_e} \vec{\nabla} \{N_1\} \bullet \kappa_e \vec{\nabla} T_e d\tau \\ + \oint_{\partial\Omega_{conv} \cup \partial\Omega_e} \{N_1\} \left[\left(\frac{h_{conv}}{\rho_{al} c_{p,al}} \right)_e (T_e - T_{amb}) \right] d\sigma \\ + \sigma \oint_{\partial\Omega_{rad} \cup \partial\Omega_e} \{N_1\} \left(f \frac{(F_{i,k},\epsilon)}{\rho_{al} c_{p,al}} \right)_e \left[T_e^4 - T_{sky}^4 \right] d\sigma \\ + \oint_{\partial\Omega_{flux} \cup \partial\Omega_e} \{N_1\} \left(\frac{\mathbf{f}(t) \bullet \mathbf{n}}{\rho_{al} c_{p,al}} \right)_e d\sigma \end{array} \right] \\
& = \{0\}
\end{aligned}
\tag{2.10}
$$

where S denotes the finite element assembly procedure carrying local element entries into the global matrix array, and M is the number of elements in the discretized domain. Note in Eq. (2.10) that all integrals are now formed on the *generic* element domain Ω_e and/or its boundary segment $\partial\Omega_e$ pertinent to BC imposition. These computed contributions are matrix row-added to form the global algebraic statement via the finite element *assembly operator*, denoted S_e^M in Chapter 4 from text [2].

Inserting Eq. (2.10) into the time Taylor Series (TS) Eq. (2.7) and into the iteration statement Eq. (2.8) does not alter their essence, hence the computable *fully discrete* $\mathrm{GWS}^h + \theta\mathrm{TS}$ algorithm for Eq. (2.1). The thermo physical properties $(\rho c_{p,al})_e$ and $\mathrm{k}_{e,al}$ are the only integrand data in Eq. (2.10) that are constants on an element Ω_e. Substituting the $T_e(\mathbf{x}, t)$ definition Eq. (2.9) into Eq. (2.10) the compute operations defined in Eq. (2.8) for Eq. (2.7) are

$$
[M] = \int_{\Omega_e} \{N_1\} \{N_1\}^T d\tau \tag{2.11}
$$

$$\{RES\}_e = \int_{\Omega_e} \vec{\nabla}\{N_1\} \bullet \vec{\nabla}\{N_1\}^T d\tau \{T\}_e - \left(\frac{1}{\rho_{al} c_{p,al}}\right) \int_{\Omega_e} \{N_1\}\{N_1\}^T d\tau \{SRC\}_e$$
$$+ \left(\frac{1}{\rho_{al} c_{p,al}}\right)_e \oint_{\partial\Omega_{con}\cap\partial\Omega_e} \{N_1\} h_{conv,e} \{N_1\}^T d\sigma [\{T\}_e - \{T_{amb}\}]$$
$$+ \left(\frac{\sigma}{\rho_{al} c_{p,al}}\right)_e \oint_{\partial\Omega_{rad}\cap\partial\Omega_e} \{N_1\} f(F_{i,k}, \epsilon) \{N_1\}^T d\sigma \left[\{T\}_e^4 - \{T_{ref}\}^4\right]$$
$$+ \left(\frac{1}{\rho_{al} c_{p,al}}\right)_e \oint_{\partial\Omega_{flux}\cap\partial\Omega_e} \{N_1\}\{N_1\}^T d\sigma \{\mathbf{FLX}_e\}_e \bullet \mathbf{n} \tag{2.12}$$

$$[JAC(\{T\})]_e \equiv \frac{\{\partial F(\{T\})\}_e}{\partial \{T\}_e} = [M]_e + \theta \Delta t \frac{\partial \{RES\}_e}{\partial \{T\}_e} \tag{2.13}$$

In Eq. (2.12), $\{SRC\}_e$ (first line), $\{conv\}_e$ (second line), $\{rad\}_e$ (third line) and the vector dot product $\{\mathbf{f}\}$ (terminal line) contain the nodal degrees of freedom (DOF) generated by interpolation of source and BC data in Eq. (2.1) using the $k = 1$ trial space basis on Ω_e. The matrix $\{T\}_e$ contains the fully discrete finite element solution approximation DOF and note that all DOF are assumed time dependent. $\mathrm{F}_{i,k}$ is to be detailed in the upcoming Section for radiosity.

2.4 Constitutive Closure for Convection BCs

Evaluating the first line of $\{RES\}_e$ in Eq. (2.12) is standard Finite Element (FE) practice. The distribution of element-dependent BC data requires identifying the corresponding constitutive closures. Correlations for the heat transfer coefficient $h_{conv,e}$ on the balance of natural forced convection are available in functional form as Eq. (2.14), see Table 2.1 for parameters, also see [4].

$$h_{conv,e} = h\left(k_{air}, Re, Pr, Gr, L^{-0.5}\right) Nu = \frac{hL}{k} = C_1 (ReGr)^n \tag{2.14}$$

Therein $\mathrm{Re} = \rho U x/\mu$ and $\mathrm{Pr} = (\mu c_{p,air})/k_{air}$ are the exchange fluid Reynolds and Prandtl numbers, $\mathrm{Gr} = (\rho^2 \beta_{air} g T L_c^3)/\mu^2$ is the exchange environment Grashof

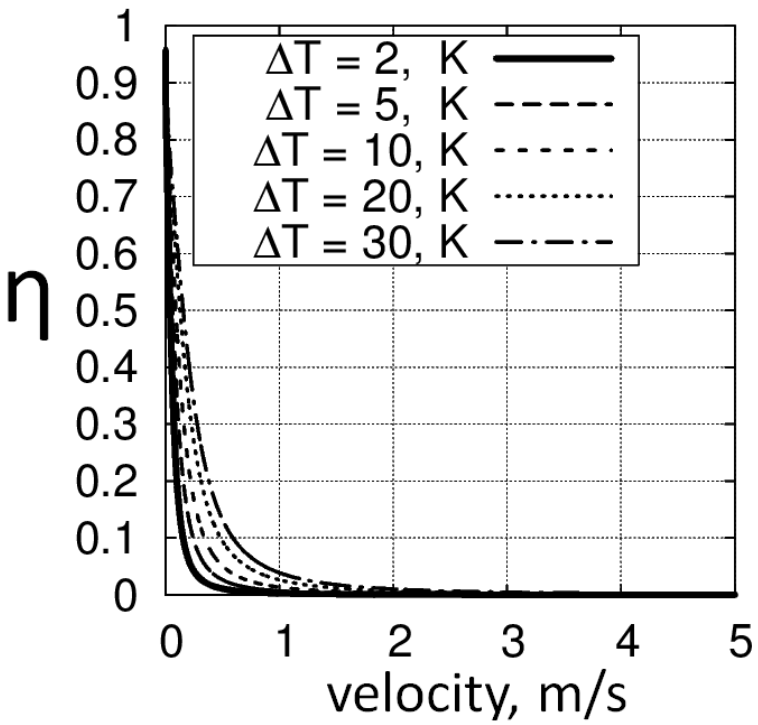

Figure 2.1: Switching term η, in convection.

number and x is distance from onset flow impingement Figure 1.7,red arrow. The natural convection characteristic length scale is suggested from literature [4] as L_c = 4Area/perimeter. A linear combination of natural and forced convection is controlled by a switching term called η_{air} a logarithmic ratio of buoyancy terms in Grashof and turbulence terms appearing as Reynolds number. Temperature potential ΔT drives the buoyancy term in Gr and U determines turbulence appearing in Re. Figure (2.1) then details the input parameters Δ T and U on η_{air}. Low velocities with high Δ T increase the switching term while low Δ T and high U reduces η_{air}. The occurrence of forced/mixed/natural convection heat transfer mode is determined by the parameter η_{air} being of $\mathcal{O}(\ll 1, \sim 1, \gg 1)$, Figure 2.1.

Environmental considerations *must* be given to the grass underneath the horizontal plates in Figure 1.1. The grass hinders the free stream velocity underneath the plate surface and therefore reduces the effective convection coefficient under the plate.

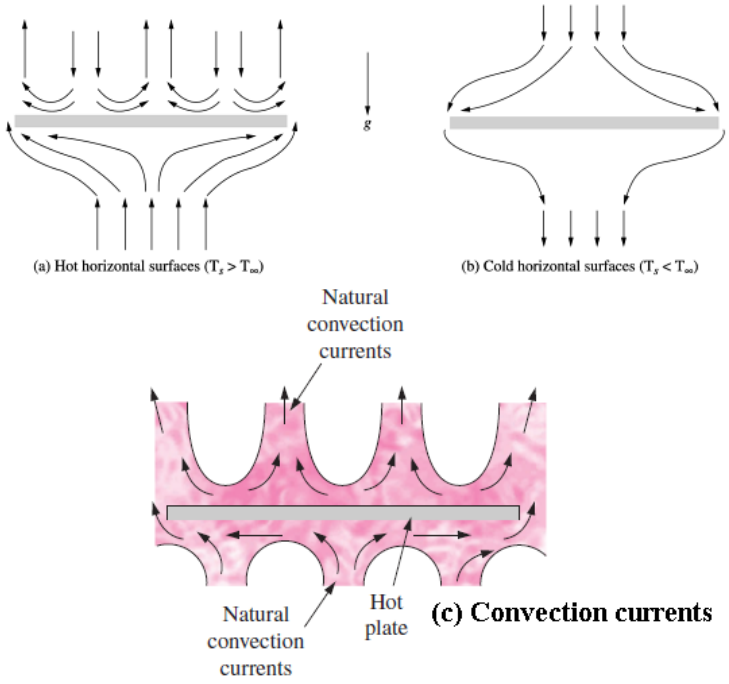

Figure 2.2: Illustration of convection currents from cooling plate (a) heating plate (b) and cartoon illustrating the convection currents (c)[3].

Therefore the plate forced convection coefficient must be reduced under the plate. A plot of h_{conv} is given in Figure 2.3.a assuming equal forced convection on both sides, but Figure 2.3.b shows affects of reduction in h_{forced}. Reasoning for reducing the forced convection will be given in Section 4.1.

Determination of Re requires input of the immersion velocity vector component tangent to the target surface. Figure 2.2 illustrates the fluid flow field associated with natural convection, and Figure 2.4 graphs the companion forced convection flow field. The velocity distribution U($\mathbf{x}$,t) of the former is of boundary layer type while that for the latter is a wall jet. The mixed convection mode is modeled as an algebraic transition within, and in all cases the Reynolds number Re is small enough such that the velocity profiles upon which the correlations are based correspond to *laminar flow*.

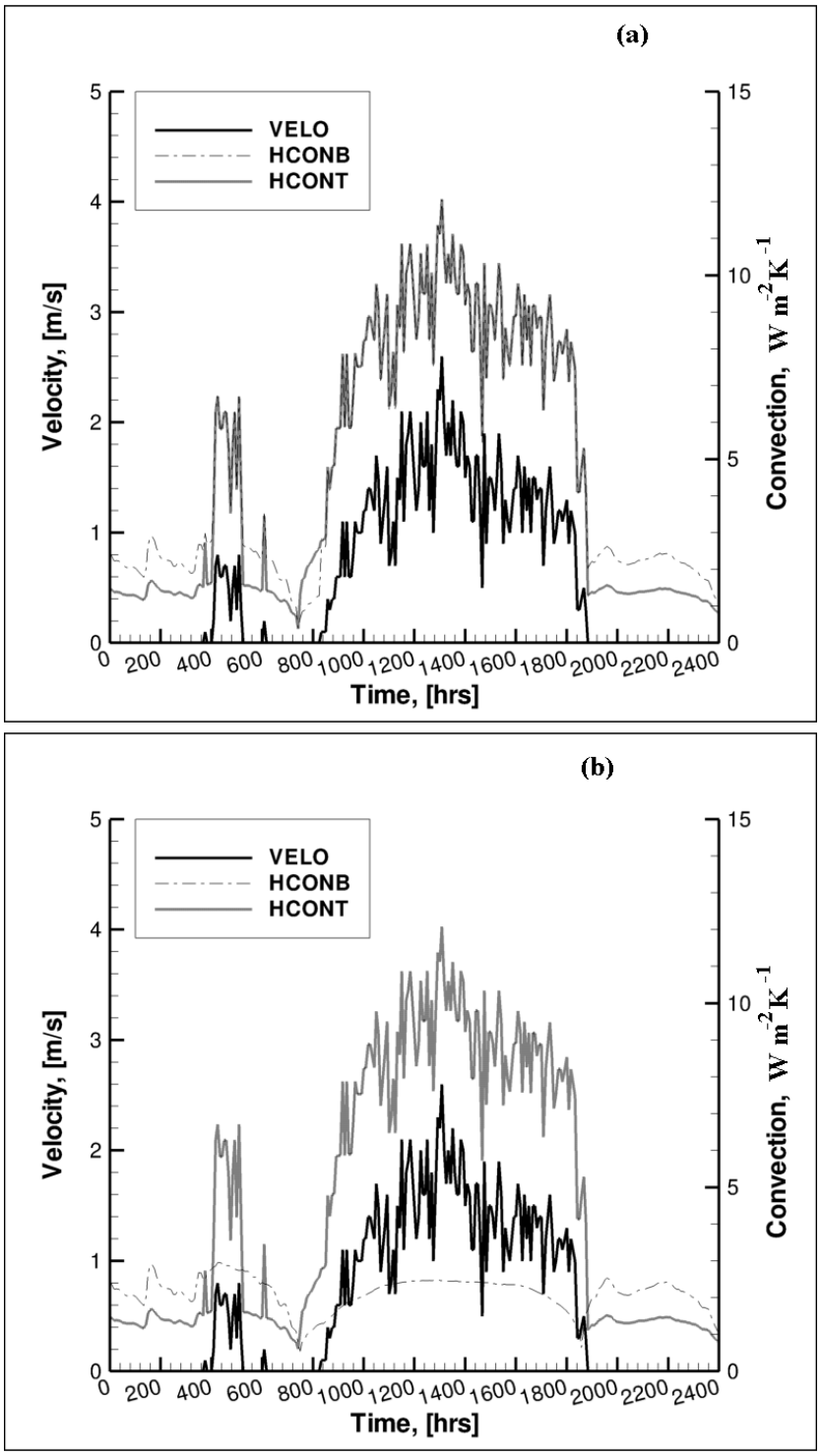

Figure 2.3: Top details equal forced convection on top and bottom, bottom details convection (off) underneath plate.

Table 2.1: Constants and computed convection data.

Forced convection	$h_{for} = C_1 k Pr^{\frac{1}{3}} Re^{\frac{1}{2}} L^{-1}$
Forced conv. coeff.	$C_1 = 0.644$
Natural convection	$h_{nat} = C_2 k (GrPr)^n L^{-1}$
Eta switching term	$\eta_{air} = Log(1 + Gr/Re^2)/(1 + Log(1 + Gr/Re^2))$
top, cooled	$C_2 = 0.540$
top, heated	$C_2 = 0.270$
bottom, heated	$C_2 = 0.270$
bottom, cooled	$C_2 = 0.150$
top, heated/cooled	$n = 1/4$
bot, heated	$n = 1/3$
bot, cooled	$n = 1/4$
mixed convection	$h_{conv} = h_{nat} * \eta_{air} + h_{for}$

Convection mechanism on Bobcat Salmon depend on many factors such as (1) if the plate is being cooled by ambient fluid Figure 2.2.a, (2) if the plate is being heated by ambient fluid Figure 2.2.b, (3) orientation of the plate all are also considered in modeling convection mechanisms. Buoyancy affects for cooled plate are hindered underneath, and the bottom side therefore retains half the proportionality (C_2) as the top Table 2.1. Also note, the exponent term (labeled as n) appearing in Table 2.1 also depends on the state of the horizontal plate as being cooled or heated by ambient air.

The *optimal* real time option for U($\mathbf{x}$,t) determination in Re Eq. (2.14), is to solve the Navier-Stokes (NS) mass conservation principle assuming the target washing velocity field is inviscid irrotational as seen in Figure 2.3,bottom. The fluid dynamics categorization is *potential theory* which generates a velocity vector *always tangent* to any solid surface and details the typical rotation and shear along the solid horizontal surface ensuing the turbulent behavior [4]. Since theory, by definition, does not admit turbulence, $\mathbf{u} \equiv -\vec{\nabla}\,\phi$ the Navier Stokes (N.S.) mass conservation PDE + BC system

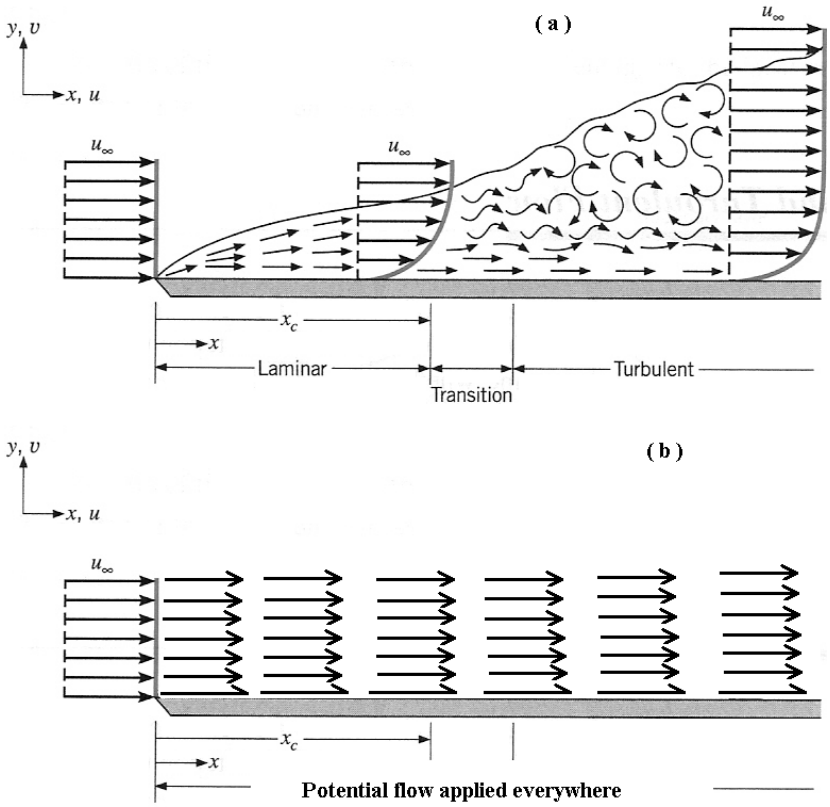

Figure 2.4: Boundary layer flow versus potential flow practice.

implementation is:

$$\begin{aligned} L(\phi) &= -\vec{\nabla} \bullet \vec{\nabla}\phi = 0 \\ l(\phi) &= \vec{\nabla}\phi \bullet \ \mathbf{n} \ - \ \mathbf{u} \ \bullet \ \mathbf{n} \ = 0 \end{aligned} \tag{2.15}$$

The Galerkin weak form for the linear PDE Eq. (2.15) follows the developed recipe. Upon completion the computable matrix statement is

$$GWS^h = S_e^M \begin{bmatrix} \int_{\Omega_e} \vec{\nabla}\{N_1\} \bullet \vec{\nabla}\phi d\tau \\ + \int_{\partial\Omega_{flow}\cap\partial\Omega_e} \{N_1\} \ \mathbf{U}(t) \bullet \ \mathbf{n} \ d\sigma \end{bmatrix} = \{0\} \tag{2.16}$$

yielding the element-level compute statement

$$\begin{aligned} \{RES\}_e = &\int_{\Omega_e} \vec{\nabla}\{N_1\} \bullet \vec{\nabla}\{N_1\} d\tau \{\phi\}_e \\ &+ \int_{\partial\Omega_{flow}\cap\partial\Omega_e} \{N_1\}\{N_1\}^T d\sigma \{ \ \mathbf{U} \ \bullet \ \mathbf{n} \ \}_e \end{aligned} \tag{2.17}$$

The solution to Eq. (2.16) generates the potential function approximation DOF $\{\phi\}$, hence ϕ^h. This approximation must be converted into velocity vector distribution, accomplished via a weak form written on the definition $\mathbf{u}^h \equiv -\nabla\phi^h$

$$GWS^h\left(u_i^h\right) = S_e^M \left[\int_{\Omega_e} \{N_1\} \left(u_i^h + \frac{\partial\phi^h}{\partial x_i}\right) d\tau\right] = \{0\} \tag{2.18}$$

the compute statement for which is

$$\begin{aligned} \{RES\} = &\int_{\Omega_e} \{N_1\}\{N_1\}^T d\tau \{\phi\}_e \\ &+ \int_{\Omega_e} \{N_1\} \vec{\nabla}\{N_1\}^T d\tau \{\phi\}_e \end{aligned} \tag{2.19}$$

Since $\mathbf{u}^h \equiv -\vec{\nabla}\phi^h$ *is not* a PDE no BCs are pertinent or required for Eq. (2.19).

The final algorithm step is to generate the scalar magnitude $\|\mathbf{U}\|$ of the velocity vector solution $\mathbf{U}^h$ from Eq. (2.19). Since $\mathbf{U}^h$ is target surface tangent, for every node on the target surface discretization the vector operation is $\equiv \sqrt{\mathbf{u}^h \bullet \mathbf{u}^h}$. All data in Table 2.1 are distributed on the discretized geometry, hence element-dependent, as are 1/x and ΔT. Consistent with the node-based formulation $\mathrm{h}_{conv,e}$ is required distributed on Ω_e. The standard FE practice is interpolation via the trial space basis, hence $\mathrm{h}_{conv,e} = \{N_1\}^T \{h_{conv}(t)\}_e$ in terms of the nodal DOF(i.e. distributed on the element nodes). In Eq. (2.12), the element matrix statement contribution is then

$$\left(\frac{1}{\rho_{al} c_{p,al}}\right)_e \int_{\partial\Omega_{conv}\cap\partial\Omega_e} \{N_1\} h_{conv,e} \{N_1\}^T d\sigma \left(\{T\}_e - \{T_{amb}\}\right)$$
$$\Rightarrow \left(\frac{1}{\rho_{al} c_{p,al}}\right) \{h_{conv}\}_e^T \int_{\partial\Omega_{conv}\cap\partial\Omega_e} \{N_1\} \{N_1\} \{N_1\}^T d\sigma \left(\{T\}_e - \{T_{amb}\}\right) \tag{2.20}$$

Since h_{conv} is precomputed data carried over from the previous time station temperature, T_{n-1}, h_{conv} becomes a constant at the current time station n. The coefficent h_{conv} is therefore implied as constant in the terminal line of Eq. (2.20) and pulled out of the integrand. The term computed in Eq. (2.20) being the nodal DOF of heat dissapated by the immersion flow field [2] pp. 107, see Eq. (6.65).

2.5 Constitutive Closure for Radiation BCs

2.5.1 Gebhart factor

Lambert's cosine law applies for shape factors for the geometry shown in Figure 2.5 given in Eq. (2.22). The shape factor or viewfactor [5] contains the kernel appearing in Eq. (2.21). View factor presents the amount of energy received from a surface facet dA_i emitted from a differential area dA_k in respect to the orientation of the surface normals and inversely proportional to the distance. The integral relation of all surface facets seeing facet i is given by

$$F_{k\to i} \equiv \frac{1}{A_k}\int_{A_k}\int_{A_i} \frac{cos\left(\phi_k\right) cos\left(\phi_i\right) dA_k dA_i}{\pi r_{k\to i}^2} \tag{2.21}$$

Terms appearing in Eq. (2.21) dA_k and dA_i are the differential areas of surfaces k and i, ϕ_k and ϕ_i are the angles between the unit normals **n** and to surface differential elements dA_k and dA_i and the vector, r, between those differential elements, and r is the length of that vector. The kernel appearing in Eq. (2.21) exhibits the symmetry property

$$K_{k\to i} = \frac{cos\left(\phi_k\right) cos\left(\phi_i\right)}{\pi r_{k\to i}^2} = K_{i\to k} \equiv K_{k,i} \tag{2.22}$$

which leads to the identities $\mathrm{F}_{k\to i} = \mathrm{A}_i\ \mathrm{K}_{i\to k}$ and $\mathrm{F}_{i\to k} = \mathrm{A}_k\ \mathrm{K}_{i\to k}$. These are valid only for differential areas, as in Figure 2.5, which generates the theoretical requirement for the node-based discrete construction.

The energetic balance for gray body radiation exchange for surface i assuming Kirchoff's law $\alpha_i = \epsilon_i$ and averaged properties (spectral absorption and reflection)

$$absorbed + reflected + transmitted = \alpha_i + \rho_i + \tau_i = 1 \tag{2.23}$$

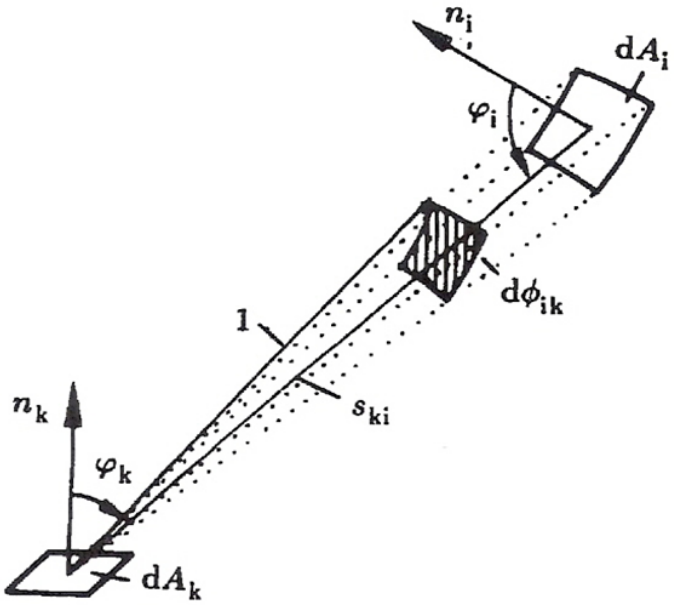

Figure 2.5: Illustration of Lambert's Cosine Law [5].

Since targets typically do not transmit incident (i.e. opaque) radiation, $\delta = 0$ leads to $\rho = 1 \;\; \alpha$ defining the reflected portion for ϵ the facet surface emissivity. An approach to closure with assumption of isothermal facet is the Gebhart factor formulation [6].

$$G_{k\to i} \equiv \epsilon_i G_{k\to i} + \sum_{j=1}^{n} \rho_j F_{k\to j} G_{j\to i} \tag{2.24}$$

For n gray bodies in radiation exchange Eq. (2.24) generates the order n-square dense matrix

$$\begin{pmatrix} (F_{11}\rho_1 - 1) & \rho_2 F_{12} & \cdots & \rho_n F_{1n} \\ \rho_2 F_{21} & (F_{22}\rho_2 - 1) & \cdots & \rho_n F_{2n} \\ \vdots & \ddots & \vdots & \vdots \\ \rho_1 F_{n1} & \cdots & \cdots & (F_{nn}\rho_n - 1) \end{pmatrix} \begin{pmatrix} G_{1i} \\ G_{2i} \\ \cdots \\ G_{ni} \end{pmatrix} = \begin{pmatrix} -F_{1\to i} \\ -F_{2\to i} \\ \cdots \\ -F_{n\to i} \end{pmatrix} \tag{2.25}$$

The Gebhart closure generates the weak form discrete implementation

$$\left(\frac{\sigma}{\rho_{al}c_{p,al}}\right)_e \int_{\partial\Omega_{rrad}\cap\partial\Omega_g} \{N_1\} f\left(F_{i,k},\epsilon\right)_e \{N_1\}^T d\sigma \left(\{T\}_e^4 - \{T_{rad}\}^4\right)$$
$$= \left(\frac{\sigma}{\rho_{al}c_{p,al}}\right) \int_{\partial\Omega_{rrad}\cap\partial\Omega_g} \{N_1\}\{N_1\}^T d\sigma \left(\epsilon_i \left\{T^4\right\} - \sum_{k=1}^{n} \epsilon_k G_{k\to i} \left\{T^4\right\}_{e=k}\right) \tag{2.26}$$

The $\sum$ k [...] function in Eq. (2.26) is a *very lengthy* compute operation for practical radiation exchange surface geometries. The resultant induced size of $[JAC]_e$ *broadens significantly* the global matrix $[JAC]$ bandwidth adding to compute intensity, hence Jacobian approximations which can compromise convergence.

2.5.2 An Alternative Radiosity Formulation

The alternative to Gebhart gray body construction is a *radiosity* formulation [7]. The theory is formulated on differential areas eliminating the facet uniform temperature assumption underlying Eq. (2.21), and totally eliminates the cited global Jacobian compute-intensity factor with Eq. (2.26). Referring again to Figure 2.5, that portion of radiation energy $\mathrm{R}_k\mathrm{dA}_k$, emanating into the semi-infinite half space from surface differential facet $\mathrm{R}_k\mathrm{dA}_k$, that impinges on surface differential element dA_i is

$$dR_{k\to i}dA_k = \frac{R_k dA_k cos\left(\phi_k\right)}{\pi} \tag{2.27}$$

Of this emission, the amount of radiation energy actually impinging on surface element $\mathrm{d}A_i$ located a distance r from $\mathrm{d}A_k$ is

$$\begin{aligned} dR_{k\to i} &= R_k dA_k cos\left(\phi_k\right) d\phi_{i,k} \\ d\phi_{i,k} &= \frac{dA_i cos\left(\phi_i\right)}{\pi r_{k\to i}^2} \end{aligned} \tag{2.28}$$

Direct substitution of the solid angle definition Eq. (2.28) generates the differential form of Lamberts cosine law

$$dR_{k\to i} = R_k dA_k \frac{cos\,(\phi_k)\,cos\,(\phi_i)\,dA_i}{\pi r_{k\to i}^2} \tag{2.29}$$

From energy balance Eq. (2.23), the radiation energy emanating from surface facet dA_i per unit time is the sum of self-emission, according to the Stefan-Boltzmann law, and that reflected from the generic surface element dA_k, hence

$$R_i dA_i = \epsilon_i \sigma T_i^4 dA_i + \rho_i dR_{k\to i} \tag{2.30}$$

Generalizing to n gray body surface facets and substituting Eq. (2.29) produces the radiosity algorithm *Fredholm integral equation* of the second kind [7].

$$R_i = \epsilon_i \sigma T_i^4 + \rho_i \left[\sum_{k=1}^{n} \int_{A_k} R_k \frac{cos\,(\phi_k)\,cos\,(\phi_i)\,dA_k}{\pi r_{k\to i}^2} \right] \tag{2.31}$$

where R_i denotes radiation energy per unit time per unit surface area. Of theoretical significance, the kernel Eq. (2.22) is a member of the integrand of Eq. (2.31).

The heat efflux q_i at the surface area A_i is the difference between the emanated radiation R_i and the total incident radiation from all exchange surfaces reaching A_i is

$$q_i = R_i - \sum_{k=1}^{n} \int_{A_k} R_k K_{ik} dA_k \tag{2.32}$$

Combining Eqs. (2.31),(2.32) defines the replacement for Stefan-Boltzmann in terms of the emitter *radiosity* R_i as

$$q_i = \frac{\epsilon_i}{\rho_i} \left[\sigma T_i^4 - R_i \right] \tag{2.33}$$

Algorithm completion in Eq. (2.12) for the radiosity formulation is

$$\begin{aligned}\left(\frac{\sigma}{\rho_{al}c_{p,al}}\right)_e \int_{\partial\Omega_{rad}\cap\partial\Omega_g} \{N_1\} f\left(F_{i,k},\epsilon\right)_e \{N_1\}^T d\sigma \left(\{T\}_e^4 - \{T_{rad}\}^4\right) \\ \rightarrow \left(\frac{1}{\rho c_{p,al}}\right) \int_{\partial\Omega_{rrad}\cap\partial\Omega_g} \{N_1\} \frac{\epsilon_e}{\rho_e} \{N_1\}^T d\sigma \left(\left\{\sigma \{T\}^4\right\} - \{R\}_e\right)\end{aligned} \tag{2.34}$$

and note the absence of the summation operation required in Eq. (2.26).

Implementation of Eq. (2.34) requires a nodal solution algorithm for radiosity Eq. (2.31). A Galerkin weak statement will generate the optimal algorithm for nodal DOF R_e. The radiosity algorithm is formed directly on a finite element domain Ω_e assuming $\mathrm{R}(\mathbf{x},t)_e = N_1(\mathbf{x}(\eta))^T R(t)_e$ leading to the discrete GWS^h element statement

$$\{GWS\}_{e=i} \equiv \int_{\Omega_i} \{N_1\} \begin{bmatrix} \left(\{N_1\}^T \{R\}_i - \epsilon_i\sigma \{N_1\}^T \{T^4\}_i\right) dA_i \\ -\rho_i \left[\sum_{k=1}^n \int_{\Omega_k} \frac{cos(\phi_k)cos(\phi_i)}{\pi r_{k\rightarrow i}^2} \{N_1\}^T \{R\}_k \, dA_k\right] dA_i \end{bmatrix} = \{0\} \tag{2.35}$$

Assuming the kernel distributed on differential surface facets, upon interpolating in the standard manner with DOF $\{K_{k,i}\}_e$, with italics signifying a summation index, 2.34 transitions to the computable form

$$\{GWS\}_{e=i} \equiv \int_{\Omega_i} \{N_1\} \begin{bmatrix} \left(\{N_1\}^T \{R\}_i - \epsilon_i\sigma \{N_1\}^T \{T^4\}_i\right) dA_i \\ -\rho_i \left[\sum_{k=1} n \{K_{k,i}\}_e^T \int_{\Omega_i} \{N_1\} \{N_1\}^T \{R\}_k \, dA_k\right] dA_i \end{bmatrix} = \{0\} \tag{2.36}$$

While not apparent as written, algorithm Eq. (2.36) generates a *hypermatrix* statement algebraic solution, detailed in the following Section 2.7.

The weak form algorithm matrix statement for radiosity, Eq. (2.36), on the generic surface facet is

$$det_i \left[n200\right]_i - \epsilon_i\sigma det_i \left[n200\right] \{T\}_i^4 - \{n10\} \rho_i det_i \sum_{k=1}^n det_k \{K_{ki}\}_e^T \left[n200\right] \{R\}_k = \{0\} \tag{2.37}$$

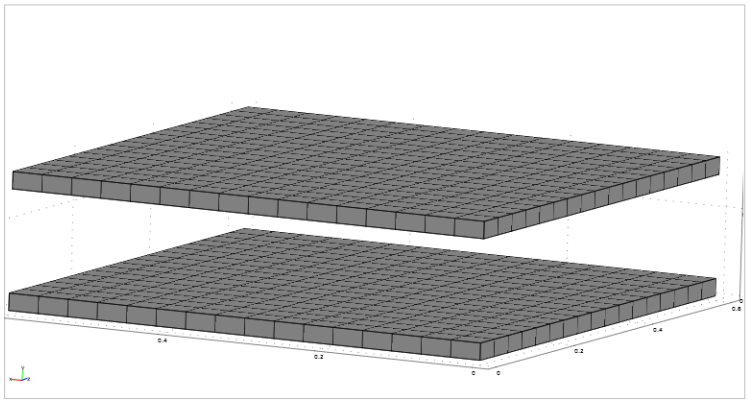

Figure 2.6: Parallel plates for radiosity exchange, M = 512 elements.

fully coupling all participating facets in a dense hypermatrix statement. Evaluating Eq. (2.37) for every participating facet generates a large linear hypermatrix statement for solution of radiosity theory DOF $\{R(t)\}$. For algebraic issue clarification, assume the kernel is a facet constant in Eq. (2.22) which eliminates appearance of the middle basis therein. This admits completing the remaining matrix product as $\{n10\}\ \{n10\}^T = [n1010]$. Now consider Figure 2.6 is a pair of facing finite area quadrilateral facets each possessing four DOF $\{R\}_e$, one at each of the four vertices. Labeling the facets 1 and 2, the two matrix statements Eq. (2.37) are

$$\begin{aligned} i = 1 : det_1\,[n200]\,\{R\}_1 - \rho_1 K_{1,2} det_2 det_1\,[n1010]\,\{R\}_2 &= \epsilon_1 \sigma det_1\,[n200]\,\left\{T^4\right\}_1 \\ i = 2 : det_2\,[n200]\,\{R\}_2 - \rho_2 K_{2,1} det_1 det_2\,[n1010]\,\{R\}_1 &= \epsilon_2 \sigma det_2\,[n200]\,\left\{T^4\right\}_2 \end{aligned} \tag{2.38}$$

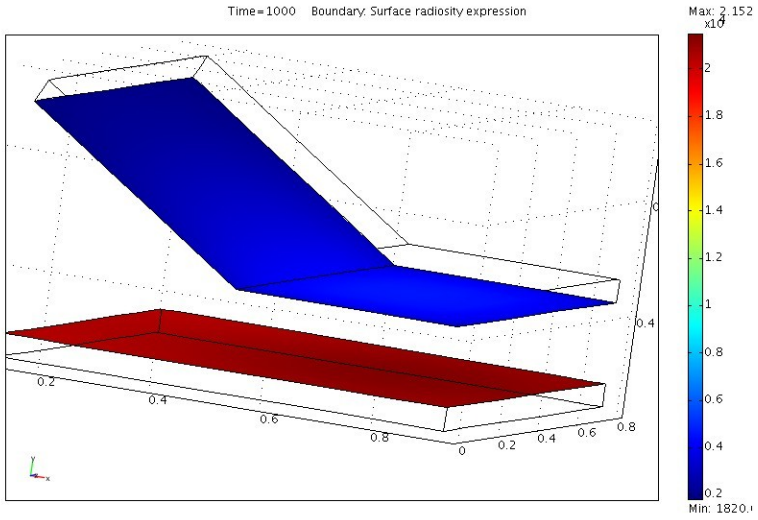

Figure 2.7: Top plate canted upwards by 30^o, radiosity solution shown from Comsol simulatin. Smoothed data!

The DOF coupling is transparent and the computable hypermatrix statement is

$$\begin{bmatrix} det_1\,[n200] - \rho_1 K_{1,2} det_1 det_2\,[n1010] \\ -\rho_2 K_{2,1} det_2 det_1\,[n1010] + det_2 det_1\,[n200] \end{bmatrix} \begin{Bmatrix} \{R\}_1 \\ \{R\}_2 \end{Bmatrix} = \sigma \begin{Bmatrix} \epsilon_1 det_1\,[n200]\,\{T^4\}_1 \\ \epsilon_2 det_2\,[n200]\,\{T^4\}_2 \end{Bmatrix} \tag{2.39}$$

The order of each global matrix is subscripted for clarity, and each algebraic equation therein is itself a matrix statement, hence the label hypermatrix.

Next bend the upper facet and discretized it into two planar facets sharing this line as in Figure 2.7. At geometric nodes thereon the temperature (algorithm assembled) DOF will be unique, i.e., identical. However the co-located radiosity DOF in $\{R\}_2$ and $\{R\}_3$ *will not be* identical due to facet kernel distinctions. Recall the viewfactor formulation given in Eq. (2.21) applied for differential facetes gives the following Eq. (2.40). The discretized surface facets appearing on surface k all see the surface facet

appearing on surface i.

$$F_{k\to i} \equiv \frac{1}{A_k} \frac{cos\left(\phi_k\right) cos\left(\phi_i\right) dA_k dA_i}{\pi r_{k\to i}^2} \tag{2.40}$$

$$\begin{bmatrix} ...\left[n200\right] - K_{1,2}...\left[n1010\right] - F_{1,3}...\left[n1010\right] \\ -F_{1,2}...\left[n1010\right] + ...\left[n200\right] - F_{2,3}...\left[n1010\right] \\ -F_{3,1}...\left[n1010\right] + F_{3,2}...\left[n1010\right] + ...\left[n200\right] \end{bmatrix} \begin{Bmatrix} \{R\}_1 \\ \{R\}_2 \\ \{R\}_3 \end{Bmatrix} = \sigma \begin{Bmatrix} ...\left[n200\right]\{T^4\}_1 \\ ...\left[n200\right]\{T^4\}_2 \\ ...\left[n200\right]\{T^4\}_2 \end{Bmatrix} \tag{2.41}$$

This observation predicts the derived weak form solution radiosity distribution will in practice be *piecewise discontinuous* as in Chapter 3.

2.6 Algorithm Completion for Solar Position

The dominant radiation flux entering in Eqs. (4.1),(4.2) is that due to the sun, a time-dependent vector. The algorithm for computation of solar position as adapted from [8]. The flux term appearing from sky diffuse $\mathbf{CG3}_{dn}$ is considered to be always pointing upward as upwelling radiation. Source of the diffuse ground radiation thus doesn't change with respect to the plate and therefore is a fixed vector. The diffuse sky radiation is considered as diffuse, and its position never changes as time of day and sky diffuse radiation is therefore also considered as a fixed position vector, pointing downward, as down welling radiation. Therefore the shortwave CM3 radiation terms are only true vectors that vary with the time of day.

The time dependent dot product between net and Cubi surface facet outward pointing unit normal vectors requires input of sun position, calculated using the solar position algorithm (SPA) detailed in [8]. The SPA fixed input arguments include month, day, year, time zone, latitude and longitude and acceptable ranges, Tables 2.3,2.2. For the Cubi experiments year = 2006, month = April, day 4 = 4, 27, time

Table 2.2: Data requirements for the SPA sun position code determination.

Description	Format	Range
Year	yyyy i.e. 1985	-2000 to 6000
Day	dd i.e. 12	1 to 31
Month	mo i.e. 8	1 to 12
Hour	hr i.e. 10	0 to 24
Minute	mm i.e. 10	0 to 59
Second	ss i.e. 12	0 to 59
Time zone (hrs)	±zz i.e. -6	12 to 12
Longitude	decimal degrees	-180 to 180
Latitude	decimal degrees	-90 to 90

Table 2.3: Algebraic computation of sun Cartesian components.

Sun's x-coordinate	$S_x = \|\mathbf{A}\|$*cos(incidenc)*sin(azimuthal)
Sun's y-coordinate	$S_y = \|\mathbf{A}\|$*cos(incidence)*cos(azimuthal)
Sun's z-coordinate	$S_z = \|\mathbf{A}\|$*cos(incidence)
Direct flux x-coord.	$F_x = \|\mathbf{CM3}_{up}\|$ * cos(incidence)*sin(azimuthal)
Direct flux y-coord.	$F_y = \|\mathbf{CM3}_{up}\|$ * cos(incidence)*cos(azimuthal)
Direct flux z-coord.	$F_z = \|\mathbf{CM3}_{up}\|$ * cos(incidence)

zone = -5, latitude 34^o, and longitude -85^o. At each solution time step the data for current hour, minute, and second must be updated.

The SPA code return arguments are sun azimuth and incidence angle in degrees, Figure 2.8. These data support computation of the resultant Cartesian coordinates for the sun, hence the vector dot products ($\mathbf{v}(t) \bullet \mathbf{n}_{Cubi\partial\omega}$). Table 2.2 details these data, where A is sun-earth separation distance and F is net CM3

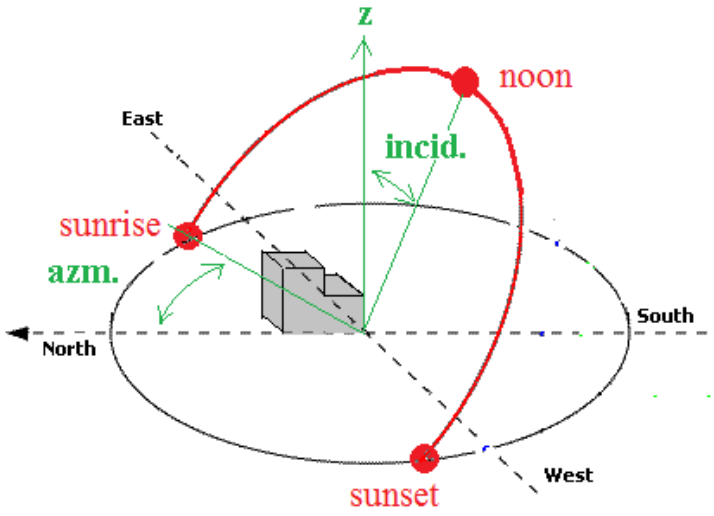

Figure 2.8: Solar position with azimuthal and incidence angle.

2.7 Weak Form Algorithm Statements for Computing

Algorithm integrals, Eqs. (2.12),(2.13),(2.35) define matrices with and without the gradient differential operator. Those without are evaluated *analytically* generating element DOF-rank square matrices with entries rational integers with the *measure* (size) of Ω_e, e.g., volume/area/length, a scalar multiplier. The measure is an integer multiple of the determinant $\det_e$ of the coordinate transformation (η , $\mathbf{x}$) to Ω_e. These integrals pervade the algorithm and evaluate to

$$\int_{\Omega_e} \{N_1\} \{N_1\}^T d\tau = det_e [m200] \tag{2.42}$$

$$\begin{aligned} \{h_{conv}\}_e^T \int \{N_1\} \{N_1\} \{N_1\}^T d\sigma \left(\{T\}_e - \{T_{amb}\}_e\right) \\ = det_e \{h_{conv}\}_e^T [n3000] \left(\{T\}_e - \{T_{amb}\}_e\right) \end{aligned} \tag{2.43}$$

$$\int_{\partial\Omega_{rad} \cap \partial\Omega_e} \{N_1\} \frac{\epsilon}{\rho_e} \{N_1\}^T d\sigma \left(\sigma \{T\}_e^4 - \{R\}^4\right) \tag{2.44}$$

$$\begin{aligned}
&\rho_i \int_{\Omega_1} \{N_1\} \sum_{k=1}^{n} \{K_{ki}\}_e^T \int_{\Omega_e} \{N_1\} \{N_1\}^T \{R\}_k \, dA_k dA_i \\
&= \{n10\} \, \rho_i det_i \sum_{k=1}^{n} det_k \, \{K_{ki}\}_e^T \, [n200] \, \{R\}_k
\end{aligned} \tag{2.45}$$

The square matrices $[m200]$ and $[n200]$, the hyper matrix $[n3000]$ and column matrix $[n10]$ are *element-independent* library data. The $\det_e$ multiplier is *element data* and depends on the dimension of Ω_e or its boundary $\partial\Omega_e$. The element matrix naming convention is:

- m denotes matrix on n - dimensional space.
- n denotes matrix on $(n$ - 1) - dimensional space.
- 2,3 indicates two, three $k = 1$ F.E. bases in the integrand.
- index pair/triple 00/000 indicates none of the bases are spatially differentiated.

The element matrix in Eq. (2.12) containing the gradient requires the (η, $\mathbf{x}$) coordinate transformation. The details of isoparameteric conversion from x to η was detailed in current work from Paul Williams [9], pages 105 to 109.

$$\kappa_e \int_{\Omega_e} \vec{\nabla} \{N_1\} \bullet \vec{\nabla} \{N_1\}^T \, d\tau \, \{T\}_e = \kappa_e det_e^{-1} \left(\frac{\partial \eta_j}{\partial x_i} \frac{\partial \eta_k}{\partial x_i} \right) [m2jk] \, \{T\}_e \tag{2.46}$$

with summation on $1 \leq$ (i,j,k) $\leq$ n with the set of DOF-order square matrices [m2jk].

In Eq. (2.12) the target ability to absorb a directed flux is limited by emissivity, recall Eq. (2.23). Noting that *diffuse* radiation interaction with the sky and ground remains, with DOF $\{T_{sky}\}_e$, the terminal form of Eq. (2.12) for the fully discrete GWS$^h + \theta$TS algorithm Eqs. (2.7), (2.11),(2.12) and now specifying the time accurate

trapezoidal rule $\theta = 0.5$, is

$$\{F(\{Q(t)\})\}_e = det_e\,[m200]\left(\{Q\}_{e,n+1} - \{Q\}_{e,n}\right) + \frac{\Delta t}{2}\begin{bmatrix} +\kappa_e det_e^{-1}\left(\frac{\partial \eta_j}{\partial x_i}\frac{\partial \eta_k}{\partial x_i}\right)_e [m2jk]\left(\{T\}_{e,n+1} + \{T\}_{e,n}\right) \\ +\left(\frac{1}{\rho c_p}\right) det_e\,\{h_{conv}\}_e^T\,[n3000]\left(\{T\}_{e,n+1} + \{T\}_{e,n}\right) \\ -\left(\frac{1}{\rho c_p}\right) det_e\,\{h_{conv}\}_e^T\,[n3000]\left(\{T_{amb}\}_{e,n+1} + \{T_{amb}\}_{e,n}\right) \\ +\left(\frac{\sigma}{\rho c_p}\frac{\epsilon_e}{1-\epsilon_e}\right) det_e\,[n200]\left(\{T\}_{e,n+1}^4 + \{T\}_{e,n}^4\right) \\ -\left(\frac{\sigma}{\rho c_p}\frac{\epsilon_e}{1-\epsilon_e}\right) det_e\,[n200]\left(\{T_{sky}\}_{e,n+1}^4 + \{T_{sky}\}_{e,n}^4\right) \\ +\left(\frac{\sigma}{\rho c_p}\right)\frac{\epsilon_e det_e}{1-\epsilon_e}\,[n200]\left(\{T_{grnd}\}_{e,n+1}^4 + \{T_{grnd}\}_{e,n}^4\right) \\ +\left(\frac{\sigma}{\rho c_p}\right)\frac{\epsilon_e det_e}{1-\epsilon_e}\,[n200]\left(\{R\}_{e,n+1}^4 + \{R\}_{e,n}^4\right) \\ -det_e\,[m200]\left(\{SRC\}_{e,n+1} + \{SRC\}_{e,n}\right) \\ +\left(\frac{\epsilon det}{\rho c_p}\right)_e [n200]\left(\{\ \mathbf{FLX}\ \}_{e,n+1} + \{\ \mathbf{FLX}\ \}_{e,n}\right) \bullet \mathbf{n} \end{bmatrix} \tag{2.47}$$

$$[JAC(\{T\})]_e \equiv \frac{\partial\{F(\{T\})\}_e}{\partial\{T\}_e} = [M]_e + \theta\Delta t\frac{\partial\{RES\}_e}{\partial\{T\}_e}$$
$$= det_e\,[m200] + \frac{\Delta t}{2}\begin{bmatrix} \kappa_e det_e^{-1}(\frac{\partial \eta_j}{\partial x_i}\frac{\partial \eta_k}{\partial x_i})\,[m2jk] \\ (\frac{1}{\rho c_p}_e) det_e\,\{h_{conv}\}_e^T\,[n3000] \\ (\frac{4\sigma}{\rho c_p}_e)\epsilon det_e\,[n200]\,diag\,[T^3]_{e,n+1} \\ (\frac{4\sigma}{\rho c_p}_e)\frac{\epsilon det_e}{1-\epsilon_e}\,[n200]\,diag\,[T^3]_{e,n+1} \\ -\left(\frac{4\sigma}{\rho c_p}\right)\frac{\epsilon^2 det_e}{1-\epsilon_e}\,[n200]\,diag\,[T^3]_{e,n+1} \end{bmatrix} \tag{2.48}$$

Recall that matrices m denotes the matrices n-dimensional space, for a 3-dimensional solution domain this admits m = 3D matrices and n = 2D matrices. Source terms appearing in Eqs. (2.47),(2.48) are volume terms use [m3000] matrices while boundary terms (surface terms) convection, radiation, radiosity, and flux use [n200] matrices [9].

In Eq. (2.47) the substitution ρ_e = 1 - ϵ_e is made. All entries in Eq. (2.48) are determined analytically from Eq. (2.47) and therein diag [•] is a diagonal square matrix containing the stated DOF on the diagonal. The last line in Eq. (2.48) is derived from Eq. (2.31).

Chapter 3

Theory, Accuracy and Convergence

Weak form theory generates error estimates in terms of H_k Sobolev norms [10]. The Sobolev norm pertinent to the energy principle Eq. (2.1) is H_1, as the trial space must contain functions with all combinations of once-differentiated products square integrable and bounded. The semi-norm of H_1 that includes the highly pertinent quadratic BC term in Eq. (2.1) is the energy semi-norm

$$\|T\|_E \equiv \frac{1}{2}\int_\Omega \left[\kappa\vec{\nabla}T \bullet \vec{\nabla}T\right] d\tau + \frac{\kappa}{2}\int_{\partial\Omega_R}\left[\frac{h_{conv}}{k}T^2\right] d\sigma \tag{3.1}$$

Under *regular* solution-adapted mesh refinement, and assuming the radiation BC nonlinearity is not pathological, the discrete approximation error $e^h(\mathbf{x},t) = \mathrm{T}(\mathbf{x},\mathrm{t}) - \mathrm{T}^h(\mathbf{x},\mathrm{t})$ for k = 1 basis GWS^h + θTS for Eqs. Eqs. (2.7), (2.11),(2.12) exhibits asymptotic convergence in the energy semi-norm as in Chapter 3 of [11]

$$\begin{gathered}\|T\|_E \leq Ch^{2\gamma}\|data\|^2_{\Omega,\partial\Omega,L2} + C_t\Delta t^{f(\Theta)}\|\{T(t=0)\}\|_E \\ \gamma = min(k=1, r-1), f(\Theta) = (2,3)\end{gathered} \tag{3.2}$$

The error magnitude at any solution time depends on the L_2 norm of the *data* driving the problem, also the energy norm of the initial condition (IC) interpolation onto the discretization DOF. C and C_t are constants (unknown), h is the measure of the mesh,

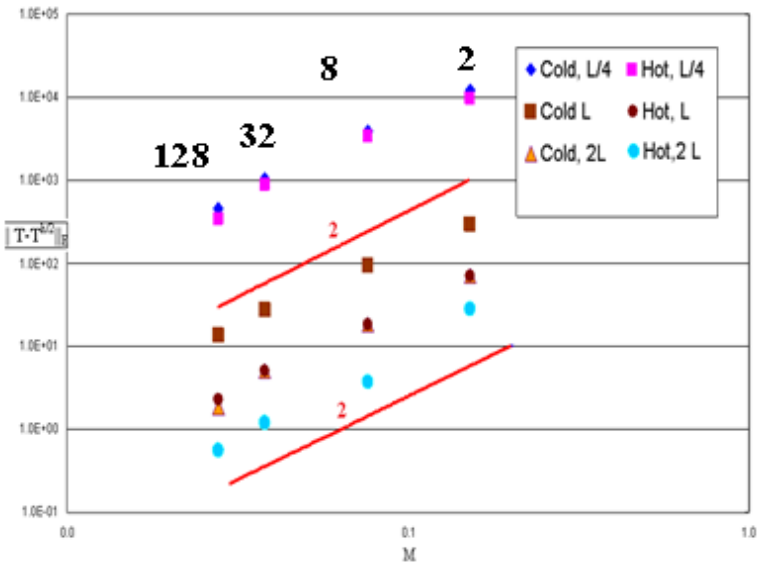

Figure 3.1: Asymptotic convergence in temperature norm, at 100 min, also shown is first four mesh refinements h,h/2,h/4,h/8.

f(Θ) = 3 for $\Theta = 0.5$ and r < k = 1 predicts *data non-smoothness* controls convergence rate. As stated, the GWS^h radiosity algorithm generates piecewise discontinuous discrete approximate solutions, hence the corresponding trial space requirement is H_0. The corresponding error estimate is

$$\left\| e^h(n\Delta t) \right\|_{H_0} \leq Ch^{k+1} \left\| data \right\|_{\partial\Omega, L2} \tag{3.3}$$

Discrete evaluation of Eq. (3.2) and that for the radiosity H_0 norm are

$$\|T\|_E \equiv \frac{1}{2} \int_\Omega \left[\kappa \vec{\nabla} T \bullet \vec{\nabla} T \right] d\tau + \frac{\kappa}{2} \int_{\partial\Omega_R} \left[\frac{h_{conv}}{k} T^2 \right] d\sigma \tag{3.4}$$

$$\|R\|_E \equiv \frac{1}{2} \left[\sum_{e=1}^{M} det_e \left\{ R \right\}_e^T \left[n200 \right] \left\{ R \right\}_e \right]^{\frac{1}{2}} \tag{3.5}$$

Confirmation of theoretical error estimates Eqs. (3.4),(3.5) validity is generated via regular mesh refinement studies for the facing parallel plate geometry in Figure 3.1.

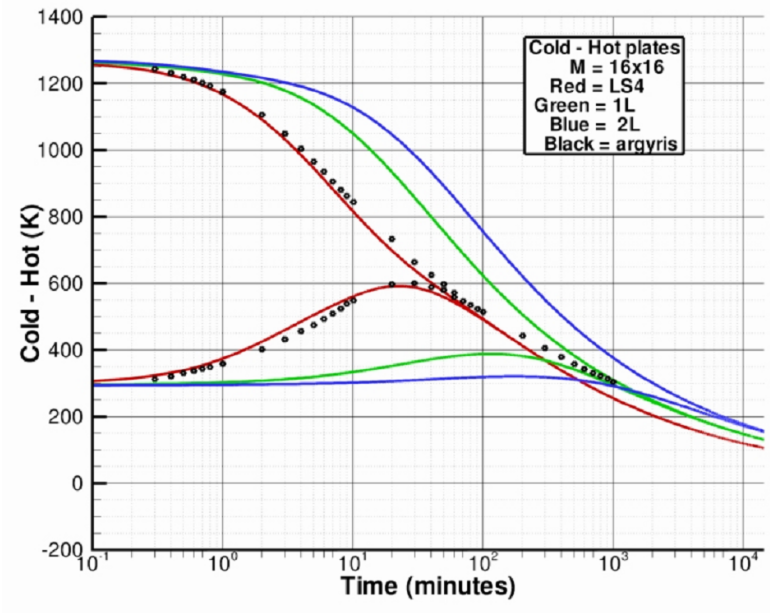

Figure 3.2: Transient temperature evolution of the parallel plates.

Plate characteristic dimension L and IC data specifications are taken from [6] with generalization to three separation distances. Figure (3.2) graphs time evolution of the temperature DOF located at each plate centroid, for each plate discretized into M = 512 elements, spanned by the quadrilateral bilinear k = 1 FE basis, for separation distances L/4, L and 2L. Verification of error estimate Eq. (3.2) for norm definition Eq. (3.4) is graphed in log scales in Figure 3.3. The symbols are computed energy norm for both plates and three separation distances at the solution time nΔt when the hot plate centroid DOF temperature is 190^{o}C. The straight lines denote a slope of two, the theoretical prediction, and clearly interpolate the data. Figure (3.4) presents the similar data for the radiosity solution DOF leading to the identical conclusion on validity of error estimate Eq. (3.5). An isolated flat plate radiosity distribution is theoretically predicted a paraboloidal surface, [6]. The GWSh algorithm indeed generates a piecewise discontinuous approximation, Figure 3.4. For plate separation distance L/4, the importance of adequately refined mesh for accuracy is summarized in Figure 3.5 as time in solution evolution at which the initially cold plate centroid

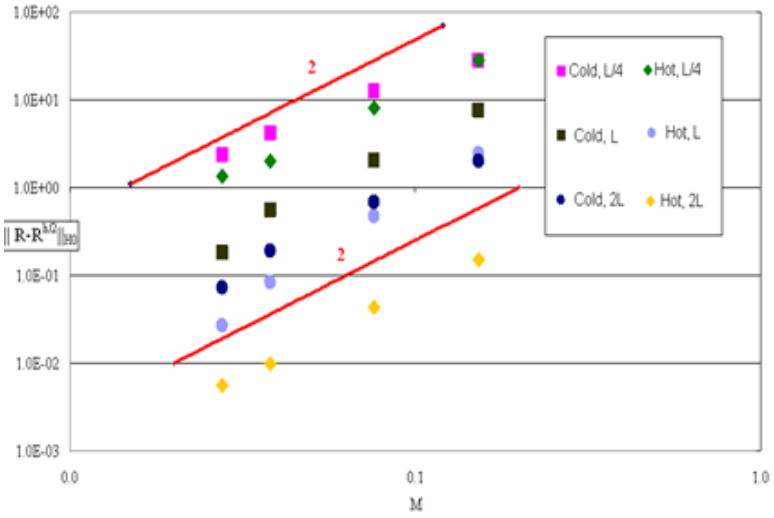

Figure 3.3: Radiosity convergence by H_0 norm.

temperature DOF extremum occurs, recall Figure 3.2. Clearly, inadequate mesh resolution delays the time of this occurrence by several minutes. The M = 128, DOF = 81 k = 1 basis mesh is the coarsest usable mesh producing a centroid temperature DOF within 1 percent of that generated by the accurate M = 512, DOF = 256 mesh solution.

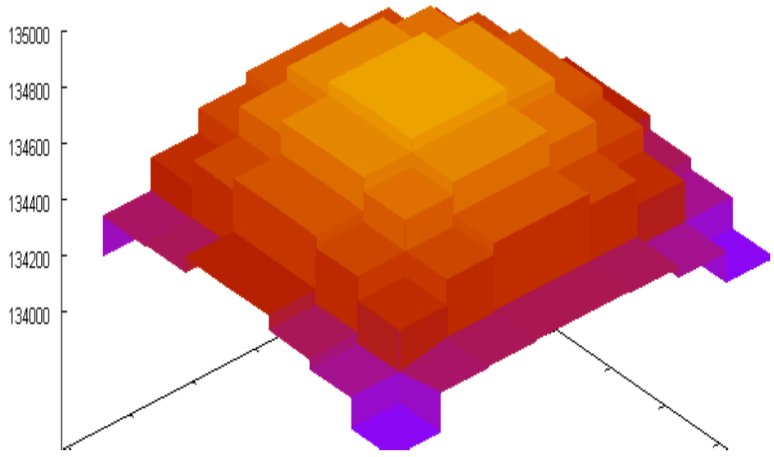

Figure 3.4: Parallel isothermal flat plat radiosity.

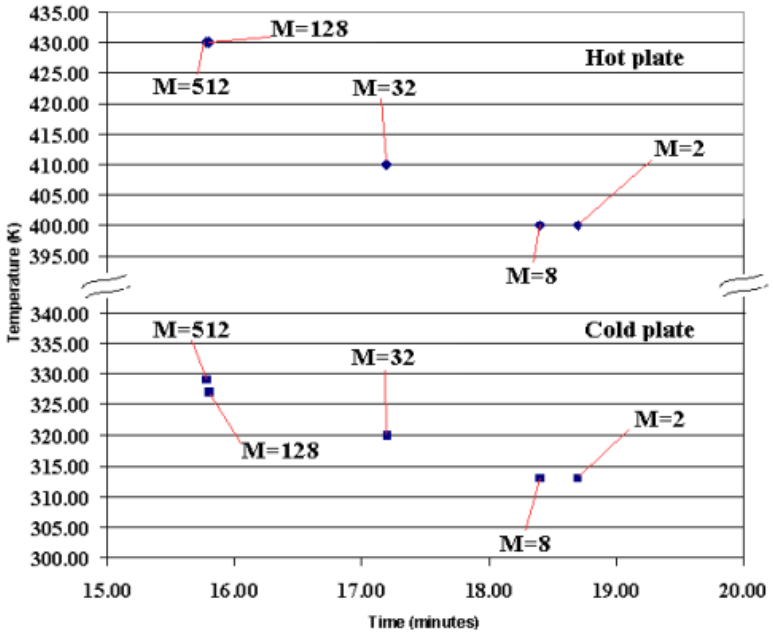

Figure 3.5: Peak temperature variation with mesh refinement.

Chapter 4

Discussion and Results

4.1 Validation of Convection BC Closure

Field data sets are recorded for diurnal radiation - mixed convection heat transfer experiments on several elementary geometries. The Bobcat Salmon experiment, [12], involves two distinct thickness aluminum flat plates, each two feet (0.6m) square and painted flat black ($\epsilon = 0.97$) posed to the environment, Figure 1.1. The field instrumentation recording radiation exposure includes long wave from the sky labeled $\mathbf{CG3}_{up}$, diffuse solar denoted PYRO and shortwave from the sun labeled $\mathbf{CM3}_{up}$, and their reflections from the ground (denoted up, down respectively), [13]. Recall the measured radiation environment is illustrated in Figure 4.1, with data recorded at 5 minute intervals over a 24 hour simulation.

The Bobcat Salmon experiment time-dependent radiation environment data set is ideal for validating closure selections for thermal convection heat transfer. Closure requires evaluating the coefficient correlations, Table. 2.1, as a function of diurnal wind field variation as it cycles the process among natural, mixed and forced convection. These data obviate the need for the radiosity algorithm hence enables the precise validation opportunity.

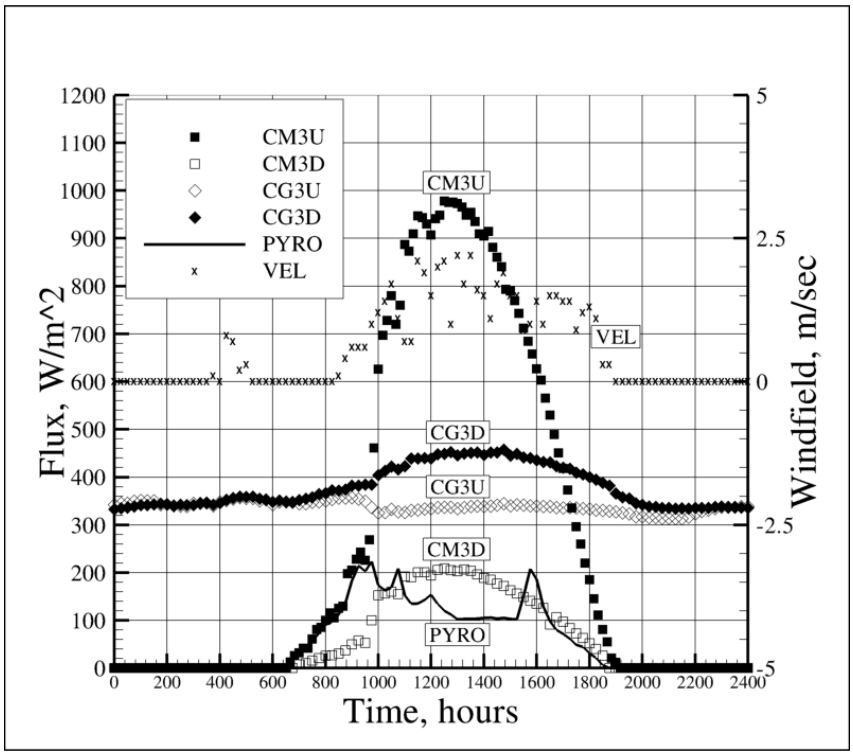

Figure 4.1: View graph of meteorological data for April 12th.

These data are single numbers the simulation imposition is uniform on each finite element of the plate discretization. Hence the algorithm degree of freedom (DOF) $\{\mathbf{FLX}\}_e \bullet \mathbf{n}$, Eq. (2.47), become the element scalar $\{\mathbf{FLX}\}_e \bullet \mathbf{n} \Rightarrow \mathbf{FLX}(t) \bullet \mathbf{n}$. Net long wave from the sky ($\mathbf{CG3}_{up}$ - $\mathbf{CG3}_{dn}$) and specular solar **PYRO** are fixed direction (upwelling or downwelling) with flux opposite to *any* surface normal $\mathbf{n}$ recall Section 2.6. Conversely, net shortwave from the sun ($\mathbf{CM3}_{up}$ - $\mathbf{CM3}_{dn}$) is the magnitude of the CM3 vector. Referring to [10] for details, the algorithm imposed flux definition becomes illustrated in Figure 2.8 and in Eq. (4.1).

$$\begin{aligned} \{\mathbf{FLX}\}_e \bullet \mathbf{n} \Rightarrow \mathbf{FLX}(t) \bullet \mathbf{n}_e &= (\mathbf{FLX}_{net}) \bullet \mathbf{n}_{\partial\Omega} \\ &= (\mathbf{CM3}_{up} \bullet \mathbf{n}) + ((\mathbf{CG3}_{up} - \mathbf{CG3}_{dn} - \mathbf{CM3}_{dn} + \mathbf{PYRO}) \bullet \mathbf{n}) \end{aligned} \tag{4.1}$$

with all data time dependent. The vector product of sun angle unit vector $\mathbf{v}(\mathrm{t})$ with plate upper surface normal $\mathbf{z}$ in Figure 2.8 is a time dependent cosine, approaching negative unity at mid-day.

Two additional diffuse radiation exchange mechanisms exist in the Bobcat Salmon experiment, both described by the Stefan Boltzmann term in BC Eq. (2.1). The plate upper surface is in radiation exchange with the sky with temperature computed from the flux data as $\mathrm{T}_{sky} \approx \left(\frac{CG3_{up}}{\sigma} \right)^{\frac{1}{4}}$. The plate lower surface is in similar exchange with the ground at temperature $\mathrm{T}_{grnd} \approx \left(\frac{CG3_{dn}}{\sigma} \right)^{\frac{1}{4}}$. To summarize, the GWS$^h + \theta$TS algorithm BC contribution to the $\{RES\}_e$ portion in Eq. (2.12), omitting time station duplication, limiting e subscript to only element-dependent data and introducing the column matrix $\{ONE\}$ to handle non-distributed experimental data, is

$$
\begin{aligned}
\{RES\}_e = & \frac{h_{conv}}{\rho_{al} C_{p,al}} det_e\,[n200] \left(\{T\}_e - T_{amb}\,\{ONE\} \right) \\
& + \Big(\frac{\sigma \epsilon}{\rho_{al} C_{p,al}} det_e\,[n200] \left(\{T\}_e^4 - T_{sky}^4\,\{ONE\} \right) \Big) \\
& + \Big(\frac{\sigma \epsilon}{\rho_{al} C_{p,al}} det_e\,[n200] \left(\{T\}_e^4 - T_{grnd}^4\,\{ONE\} \right) \\
& + \Big(\frac{\epsilon}{\rho_{al} C_{p,al}} det_e\,\{n10\} \left(\mathbf{CM3}_{up} \right) \left(\mathbf{v}(t) \bullet \mathbf{n} \right) \\
& + \Big(\mathbf{CG3}_{\ up} - \mathbf{CG3}_{dn} - \mathbf{CG3}_{dn} - \mathbf{PYRO} \Big) \left(\mathbf{z} \bullet \mathbf{n} \right) \Big)
\end{aligned}
\tag{4.2}
$$

GWS^h + θTS algorithm simulations were conducted for five different 24 hour diurnal data cycles, April 3,6,12,18,27 of 2006, and for the two distinct thickness plates, with exception that the 27^{th} using one unique thickness. For natural convection heat transfer, $\Delta T > 0$ corresponds to plate heating by surroundings while $\Delta T < 0$ denotes plate environmentally cooled. Convection heat transfer is assumed to exist on both upper and lower plate surfaces and forced convection correlation closure requires L in the Nusselt number and onset distance x to be defined in the Reynolds number Eq. (2.14).

Selecting plate dimension L $\equiv$ 0.6 m in the Nusselt number, and $x \equiv$ 0.6m in Reynolds number Eq. (2.14), the onset flow distance to the built-back TC, 24 hour plate centroid computed temperature *posteriori* data (labeled aPSE) are graphed for the one inch and one-eight inch thick plates Figure 4.2. Graphed for comparison is the built- back TC (labeled EXPT) time history, also all radiation flux data (W/m^2). Quantitative agreement between simulation and built-back TC is excellent in time period 0000 $-$ 1000 hours for both plates. Conversely, substantial disagreement between prediction and experiments exists during mid-day atmospheric heating, 1000 $-$ 1800 hours, with the algorithm prediction lower that experiment by $\pm$ 8^o Kelvin.

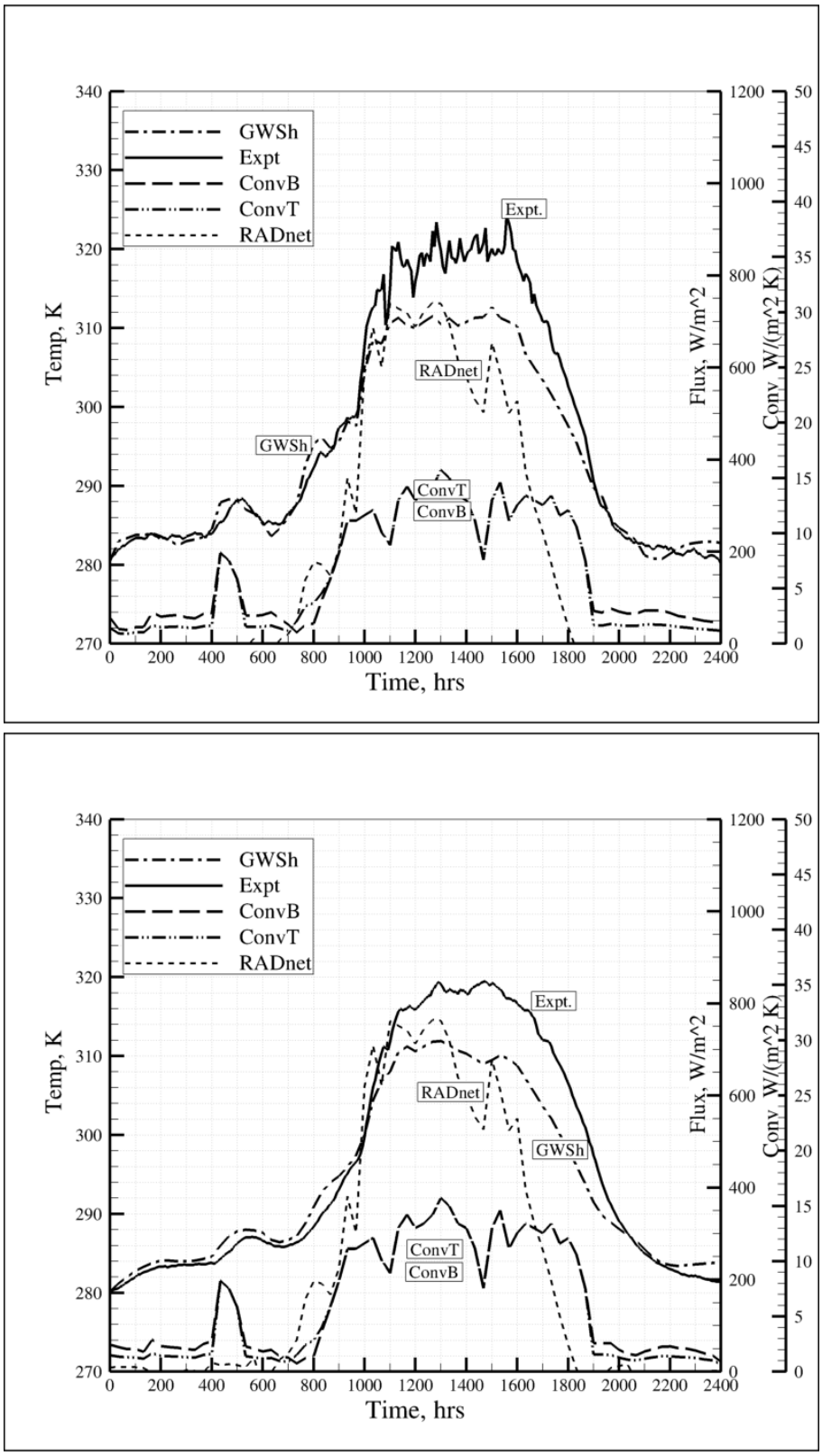

Figure 4.2: Validation data for 1 and 1/8 inch plate, and L=2x=0.6m.

Similar graph as above with exceptions of L $\equiv$ 0.6 m in the Reynolds number, and $x \equiv 0.3$m in Eq. (2.14) shown in Figure 4.3. Improvement in simulaton with disagreement between prediction and experiments exists during mid-day atmospheric heating, $1000 - 1800$ is half that of the previous assumptions in characteristic length.

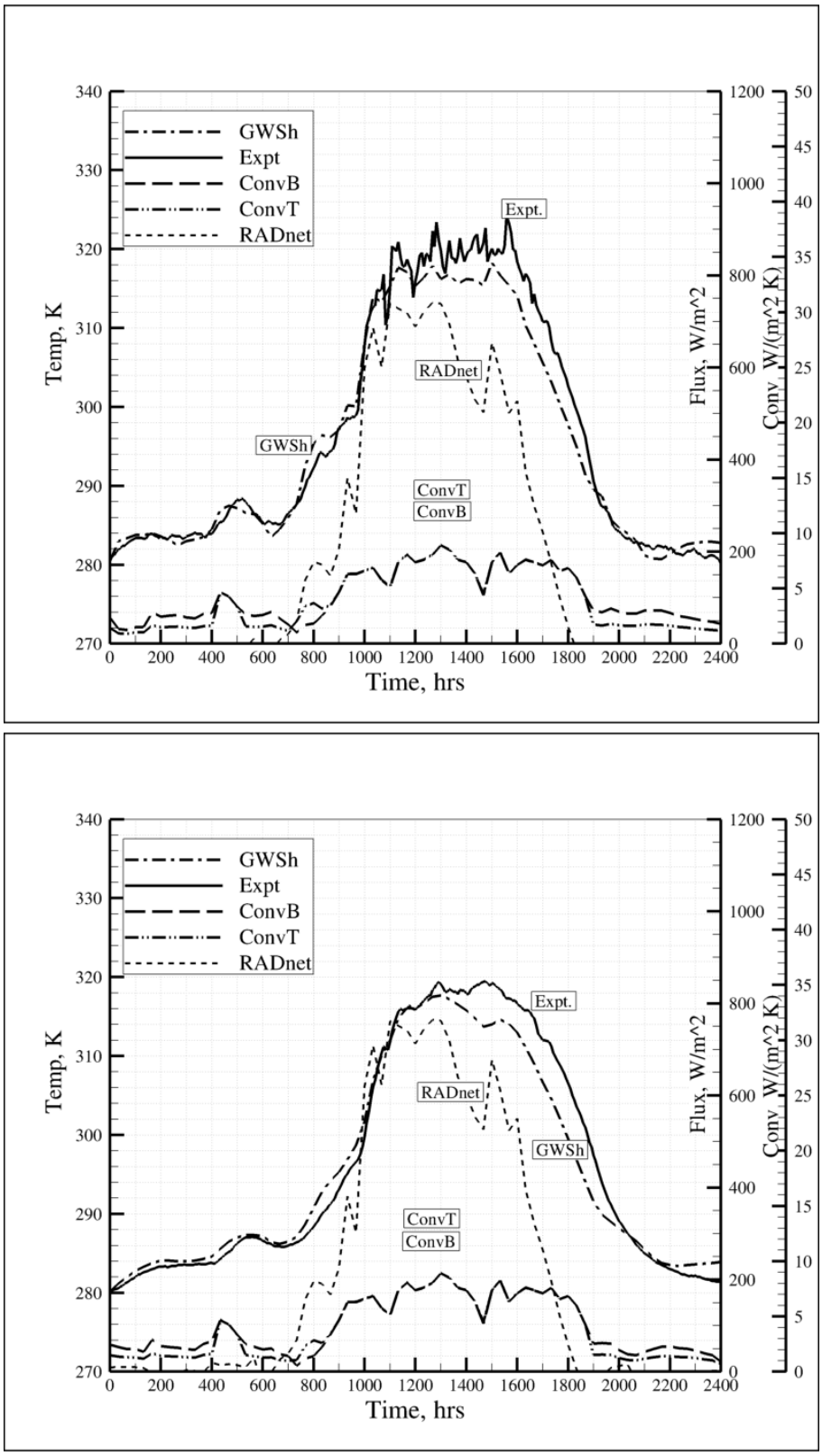

Figure 4.3: Validation data for 1 and 1/8 inch plate, and L=0.6m and x=0.3m.

This temperature disparity confirms the algorithm simulations are excessively convection cooled during the mid-day hours. Potential causes include, plate dimension x for forced convection Reynolds number is inappropriate; plate underside convection heat transfer is not as effective as on the top surface. The former is readily evaluated by halving L to match x, to the onset flow distance to the *built-back* TC. Simulations with L = 2x Figure 4.4, confirm excellent quantitative agreement during the extended period 0000 - 1400 hours for both plates (bottom left). However, substantial disagreement persists in the period 1400 - 1800 hours.

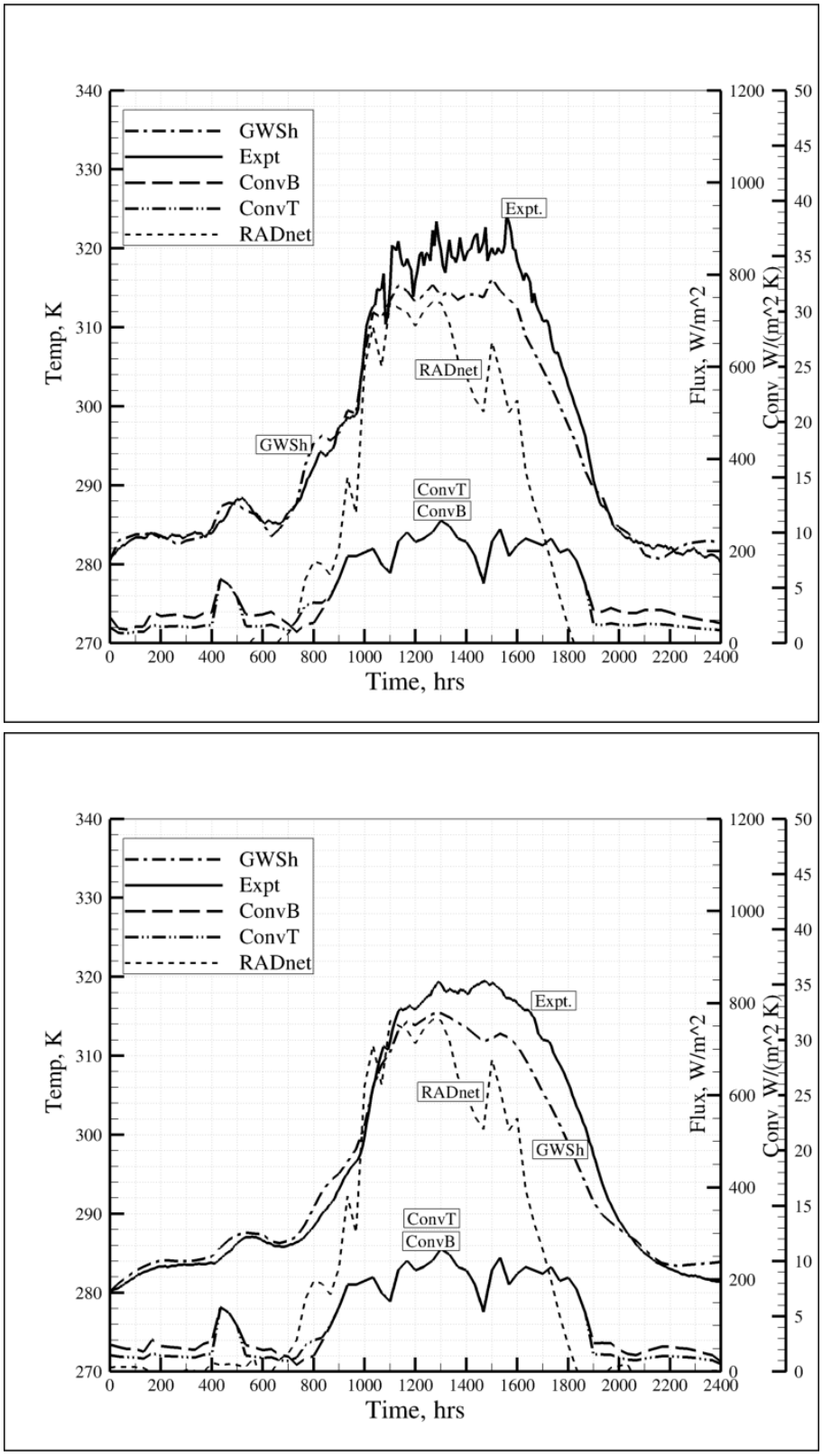

Figure 4.4: Validation data for both 1 and 1/8 inch plate, and L=1x=0.3m.

For the 1/8 and 1 inch plates the simulation predicted local temperature peak at 1800 hours is totally missing in the experimental data. This peak, directly induced by the coincident local excursion in *PYRO*, renders that data acquisition subject to question. Translating this peak to time period $1500 - 1700$ hours and repeating the simulation generates the solution graphed in Figure 4.5. The highly oscillatory mid-day experimental data is clearly reproduced in the simulation, the direct consequent of minimal thermal capacity of the 1/8 inch plate. Excellent quantitative agreement between experiment and simulation also occurs during dawn atmospheric turnover, $0400 - 0600$ hours, and with the experiment temperature oscillation peaks during $1200 - 1600$ hours. Finally, the temperature slopes during late afternoon cool down also match very well with simulation temperature at time advanced by 20 minutes.

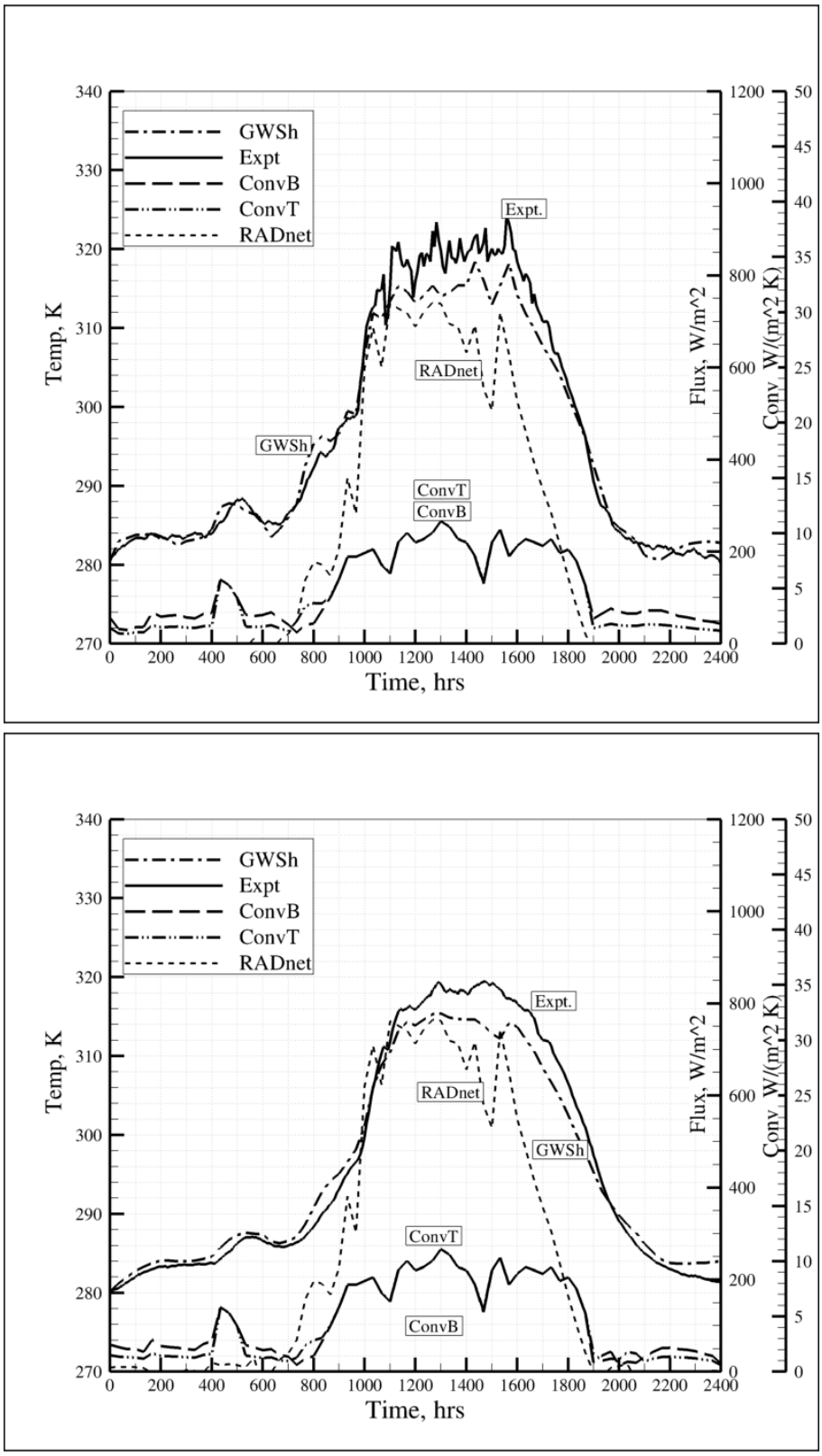

Figure 4.5: Before *PYRO* excursion in 1 inch (top) and 1/8 inch (bottom) plate, and L=2x=0.6m.

Viewing Figure 1.1, the aluminum plates are located less than one meter above ground level. The lower surface convection level assumption may be flawed, as ground heating natural convection might serve to restrict the onset flow from passage underneath the plates thus infringing on plate lower surface forced convection. Reducing this convection coefficient by half during the time period $1400 - 1800$ hours, the repeat simulation generates the temperature distribution graphed in Figure 4.6. Excellent quantitative agreement between experiment and simulation is now recorded for the entire 2400 hour experiment. Performing this data alteration for the one−eight inch thick plate during $1600 - 1900$ hours eliminates the 20 minute temperature at time disparity in Figure 4.6, yielding excellent quantitative throughout the 2400 hour period.

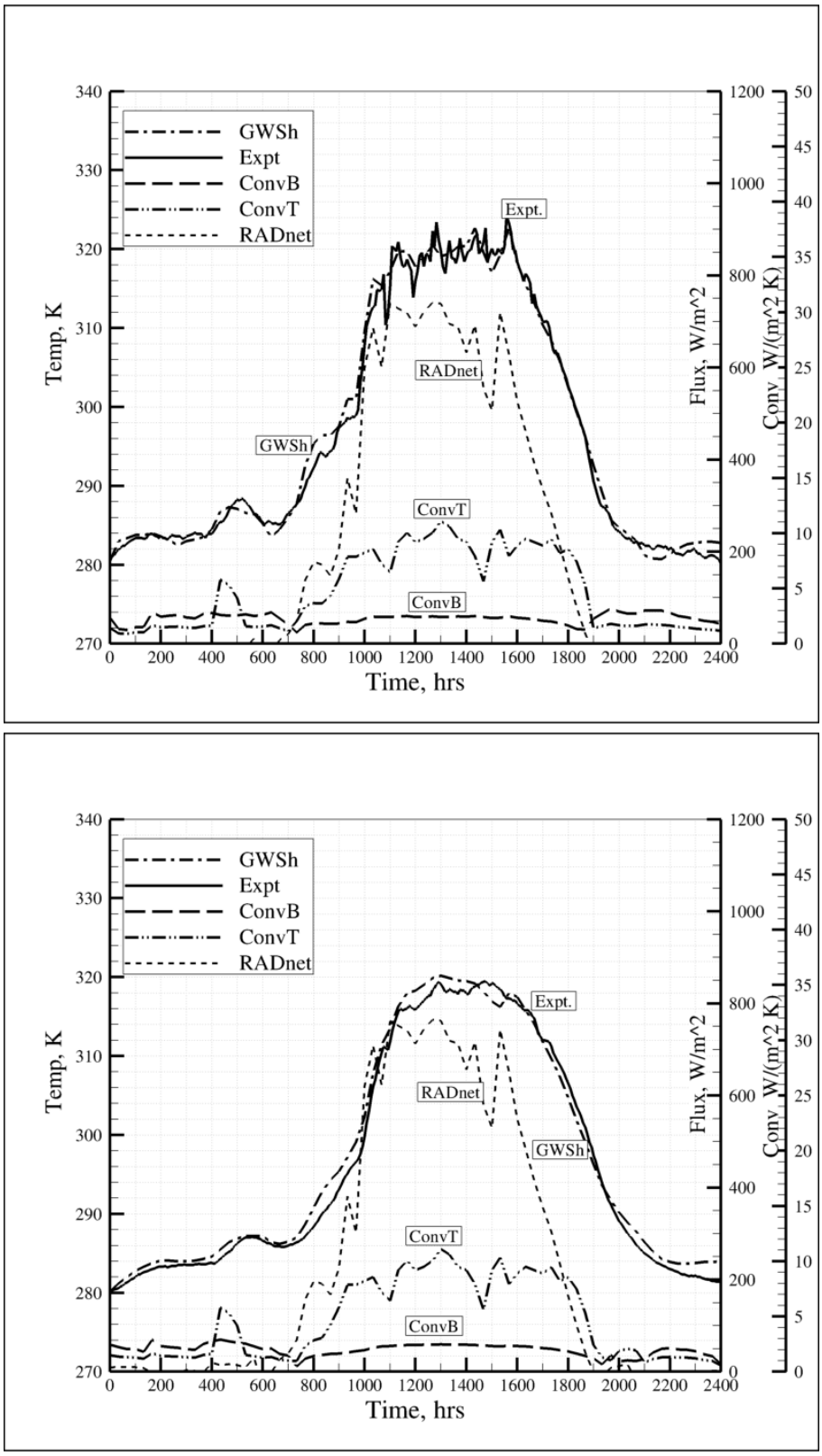

Figure 4.6: Validation data for 1/8 inch plate, no-bottom-forced, and L=1x=0.3m.

4.2 Diurnal Simulation of Cubi with Convection and Radiation

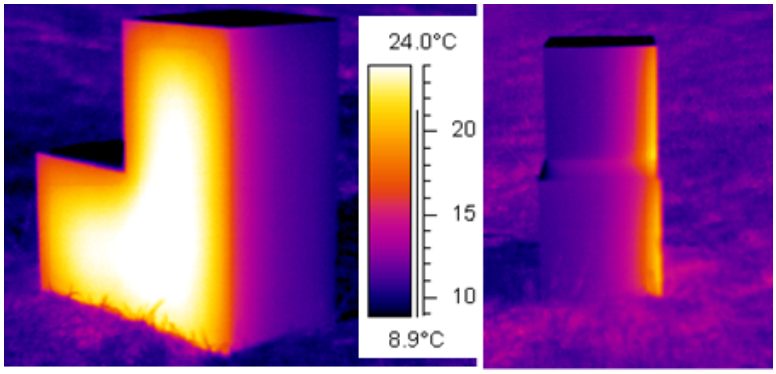

Figure 4.7: Radiometric images of Cubi side facing morning.

The Cubi test was a unique test in that the plate bottom side is adiabatic, recall Chapter 1, Figure 1.2. The April 27 2006 Bobcat Salmon experiment data are specified for the Cubi test. A 4mm thick flat green ($\epsilon = 0.93$) was also present in this experiment for which solar flux measurements, Figure 4.8, were taken. For the convection heat transfer correlation coefficient determination detailed in Section 2.4, Figure 4.9 graphs the simulation centroid temperature DOF (labeled aPSE) comparison to the April 27 experiment temperature and solar flux data.

This result, obviously in error, was traced to the level of recorded *PYRO*, Figure 4.9, top left, which exceeds that of the April 12 data base by a factor of five! The aPSE prediction also responds to the Pyro (labeled *PYRO*) signal drop out at 1630 hours, which clearly is not present in the experiment temperature data. Uniformly reducing the April 27 recorded *PYRO* data by five, but not deleting the signal drop out, generates the excellent quantitative agreement between simulation and experiment, Figure 4.9, top figures. Eliminating the *PYRO* data drop out during $1630 - 1700$ hours would further favorably impact the aPSE comparison with experiment (EXPT).

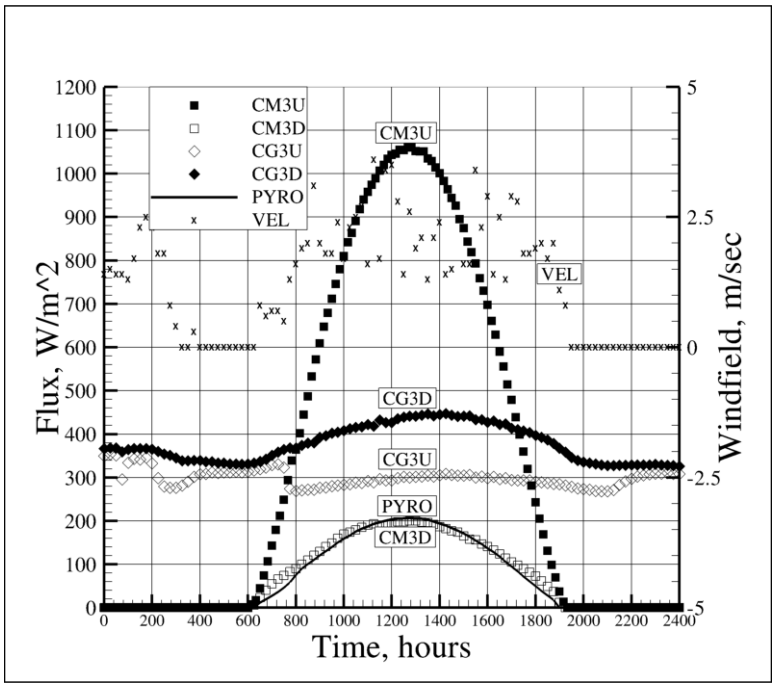

Figure 4.8: Meterological data set for 04−27.

Leftmost figures show L = x = 0.6m while rightmost figures simulated for L = x = 0.3m, and no convection applied to side.

With this vital determination, Figure 2.8 illustrates Cubi simulation direct solar and flux data specification requirements. As discussed in Section, 2.6 the experimental flux data definition remains as expressed in Eq. (4.1). Due to Cubi multiple surface facet orientations, hence the 3D immersion velocity vector field generating distinct

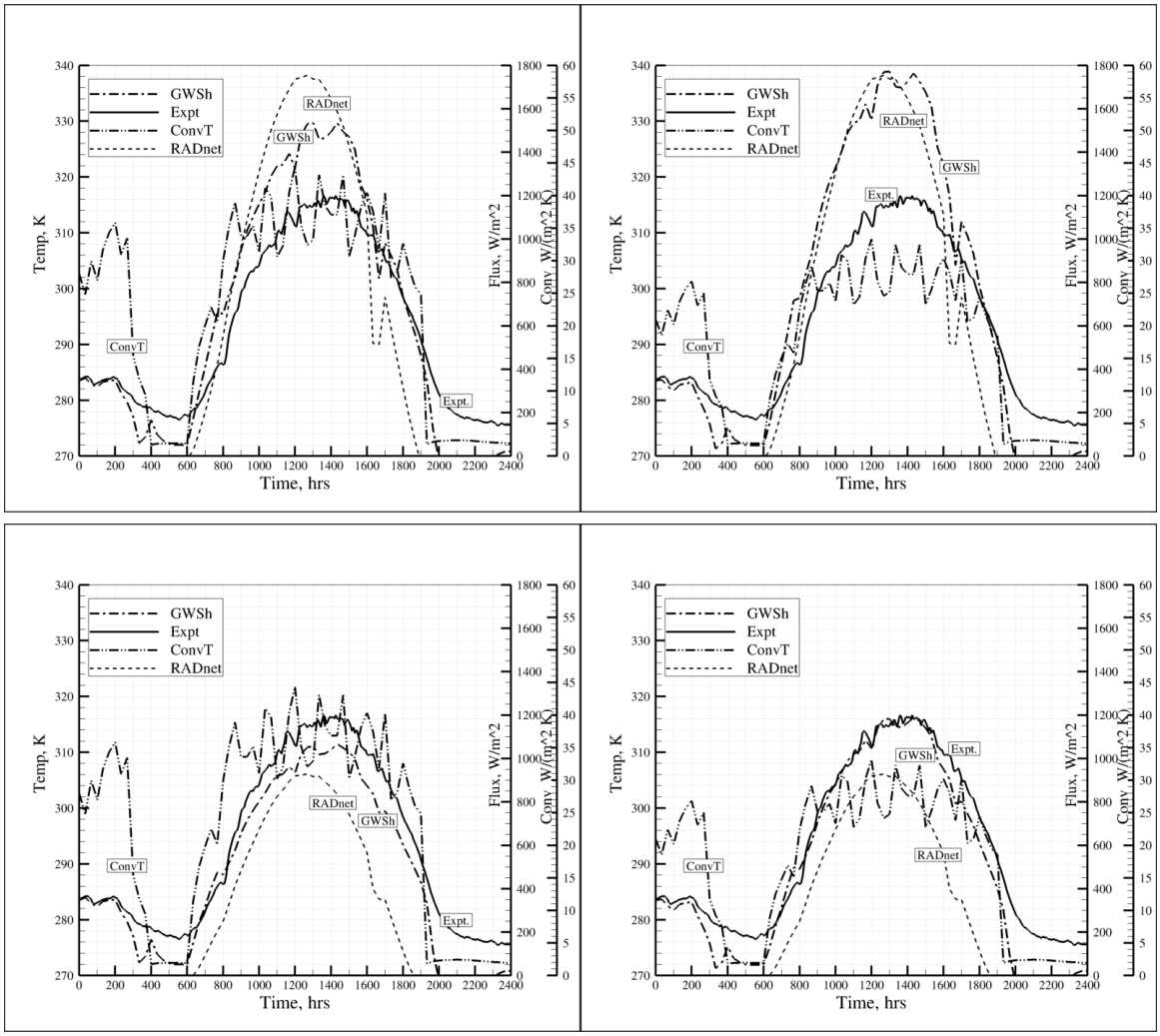

Figure 4.9: Pediction validation data for Cubi plate.

surface facet convection heat transfer distributions, Eq. (2.16) becomes altered to

$$\begin{aligned}\{RES\}_e =& \ldots \left(\frac{h_{conv}}{\rho c_p} det_e\,[n200]\,(\{T\}_e - T_{amb}\,\{ONE\})\right) \\ &+ \left(\frac{\sigma\epsilon}{\rho c_p} det_e\,[n200]\,\left(\{T\}_e^4 - T_{sky}^4\,\{ONE\}\right)\right) \\ &+ \left(\frac{\sigma\epsilon}{\rho c_p} det_e\,[n200]\,\left(\{T\}_e^4 - T_{grnd}^4\,\{ONE\}\right)\right) \\ &+ \left(\frac{\epsilon}{\rho c_p} det_e\,\{n10\}\,(\mathbf{CM3}_{up} - \mathbf{CM3}_{dn})\,(\ \mathbf{v}\ (t) \bullet \mathbf{k})\right) \\ &+ (\mathbf{CG3}_{up} - \mathbf{CG3}_{dn} - \mathbf{PYRO})\end{aligned} \tag{4.3}$$

Thermal convection heat transfer for Cubi requires prediction of the immersion velocity vector distribution, hence determination of U in Re, Table 2.1, as a function of surface facet location. The summaries of the April 27 experiment wind field direction and magnitude data are graphed in Chapter 1, Figure 1.6. The wind direction is dominantly WNW, except for the quiescent period during 0400 - 0600 hours. Necessary step to simulation is to assume an onset average at a 30^o angle, the arrow drawn in Figure 4.10. This sets the potential flow BC on the immersion flow field simulation inflow boundaries of the $n = 3$ domain surrounding Cubi.

The resultant 3-dimensional velocity vector distribution, determined via the potential theory GWS^h algorithm, Eqs. (2.2),(2.8), is summarized in Figure 4.10 as perspective graphs of velocity unit vector distribution based on lines on select horizontal planes. (Note: the lateral span of the solution domain extends well beyond these near field graphics). The color bar denoting speed in m/s is located in the bottom graphic. The onset velocity, from upper left, is slowed in approaching Cubi with largest magnitude velocity induced by the upwind Cubi corners. The vertical velocity component is essentially null; not shown is the velocity field on the Cubi

downwind face, as potential theory is incapable of accurately predicting the large recirculation zones there existent.

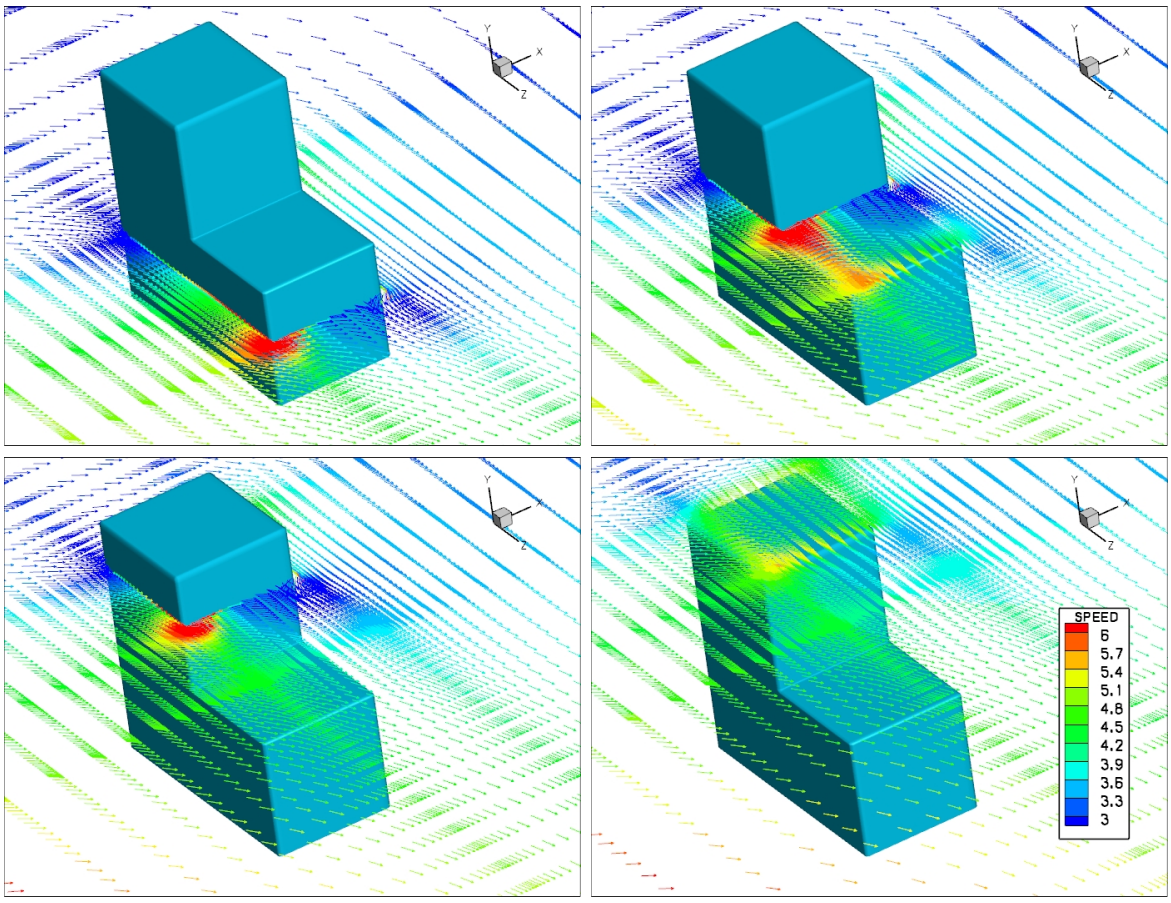

Figure 4.10: Velocity flow field, vector graph, ground up, aPSE.

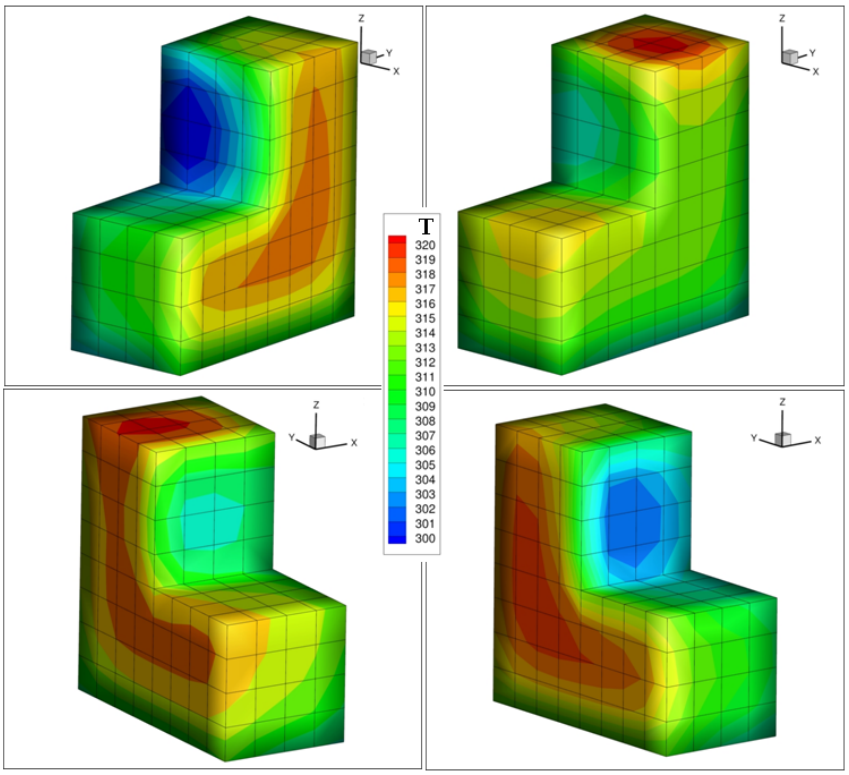

Figure 4.11: Solution data using conjugate heat transfer algorithms.

The detailed DOF array $\{h_{conv}\}_e$ accuracy requirement, Eq. (2.47) hence Eq. (4.1), was replaced by an average $\{h_{conv}\}_{\partial\Omega}$ for each Cubi surface facet, reducing the matrix from [n3000] to [n200]. Onset x was defined as the distance from stagnation line to each facet centroid with U $\equiv$ 4.5 m/s defined as the surface average speed (for onset U = 3.0 m/s, Figure 4.10. During simulation the 4.5/3.0 U proportion was algebraically altered to match measured onset wind field magnitude variation, Figure 1.6. Natural convection heat transfer was defined on all Cubi downwind surface facets. Putting convection, solar, and radiosity algorithms all together onto all Cubi surfaces is given below in Figure 4.11.

Final Cubi simulations as shown, top left Cubi at 9:00 am, top right Cubi at 12:00 pm, bottom left Cubi at 3:00 pm, and finally at bottom right 6:00 pm orientation shown for sunset. All algorithms applied.

Chapter 5

Summary and Conclusion

Extremization of a weak form for the energy conservation principle differential equation naturally implements the convection, radiation and flux Robin boundary conditions associated with unsteady prediction of target thermal signatures. Combining a spatial semi-discretization via finite element trial space basis functions with time-accurate integration generates a totally node-based algebraic statement for computing. Closure for natural-forced-mixed convection heat transfer is extracted from the literature, while that for radiation is a newly derived node-based radiosity formulation generating piecewise discontinuous solutions.

Algorithm performance is accurately predicted via identified asymptotic convergence theories. Comparison of computed a posteriori data with detailed 24 hour diurnal field experiment data, for distinct thickness flat plates and a cube-shaped three dimensional object, validate the algorithm and the identified convection and radiation heat transfer closure models.

Chapter 6

Future Prospects

Meeting the real time requirement means computing on Graphical Processing Units (GPUs). The potential performance improvement for codes or algorithms that can take advantage of the GPU's programing model and do most of their computation on the GPU is enormous. The scale up is quite a factor in considering improvement of codes running on GPU's relative to CPU's. Profiling a code will reveal parallelism. Parallelism is considered in many do loops, and computations done 1,000's of times can be a candidate to move onto the GPU. On drawback, one must also consider the data transfer between the CPU and GPU and reduce the communication. Data transfer across the bus is a bottleneck.

Adding more fidelity by adding more physics to the model. In many cases, the solution data during morning and evening hours shows some disagreement that is contributed to condensation. Adding a condensation model (evaporative cooling) to the boundaries would reduce error at the expense of adding in more data input variables such as dew point temperature, relative humidity, and barometric pressure.

The air properties can be estimated as a function of air temperature, barometric pressure, and in some cases as a function of relative humidity. Computing density, specific heat, and thermal conductivity of air as a function of these parameters improves the fidelity of the code for extreme environmental conditions. Currently all environmental values are predetermined for a median fixed temperature.

Bibliography

[1] Chen, Bing. 1991. "Determination of the Clear Sky Emissivity for use in Cool Storage Roof and Roof Pond Applications". ASES proceedings, Denver, CO.

[2] Baker, A.J. (2012) *Finite Elements*, Wiley, New York.

[3] Baker, A.J. (1983) *Finite Element Computational Fluid Mechanics*, Taylor and Francis, Pa.

[4] Incropera, Frank. (1985) *Foundamentals of Heat and Mass Transfer*, Wiley, New York.

[5] Walton, G.N. (2002). "Calculation of Obstructed View Factors by Adaptive Integration" NIST TR 6925.

[6] Miller, F.P., Vandome,A.F., and Brewster, J.M. (2010). *Gebhart Factors*, VDM Publishing House Ltd, England, ISBN 6134096326.

[7] Argyris, John; Jochen Szimmat. 1992. "An Analysis of Temperature Radiation Interchange Problems, Journal of Computer Applied Mechanics and Engineering", Vol. 94, issue 2, pp. 155-180.

[8] Redas, I; Andreas, A. 2004, "Solar Algorithm for Solar Radiation Applications", Solar Energy, Vol. 76(5), pp. 577-589.

[9] Paul T. Williams. 1993. *A Three-Dimensional, Time-Accurate Incompressible, Navier-Stokes, Finite Elment CFD Algorithm*, Dissertation, UTK.

[10] J. Tinsley Oden and Leszek F. Demkowicz. 1996. *Applied Functional Analysis (Computational Mechanics and Applied Mathematics)*, Chapman and Hall/CRC Press, pp. 576 pages.

[11] Baker,A.J. (2013) *Optimal Modified Continous Galerkin CFD*, John Wiley, London.

[12] Sanders, Jeff, August 2006, "High-resolution Ground Target Infrared Signature Modeling for Combat Target Indentification Training", Proceedings of the Ground Target Modeling and Validation Conference 13^{th}, MI.

[13] CNR 1 NET RADIOMETER, Instruction Manual 0340-300, Kipp and Zonen, Inc., New York USA.

Appendix

Appendix A

Appendix

Table A.1: Material properties for Bobcat Salmon.

Density, ρ_{al}	2700	$[\frac{kg}{m^3}]$
Specific heat capacity, $c_{p,al}$	884	$[\frac{J}{kgK}]$
Thermal conductivity, k_{al}	237	$[\frac{W}{mk}]$
Krylon paint emissivity, ϵ	0.97	[scalar]
Reflectance (IR Range)	≤ 0.001	$[\frac{W}{m^2}]$
Physical width, W	0.6084	[meters]
Physical length, L	0.6084	[meters]

Table A.2: Material properties for Cubi.

Density, ρ_{st}	7,800	$[\frac{kg}{m^3}]$
Specific heat capacity, $c_{p,st}$	460	$[\frac{J}{kgK}]$
Thermal conductivity, k_{st}	69	$[\frac{W}{mk}]$
Krylon paint emissivity, ϵ	0.93	[scalar]
Physical width, W	0.500	[meters]
Physical length, L	0.500	[meters]

Table A.3: Fluid material properties at STP.

Density, ρ_{air}	1.2000	$\left[\frac{kg}{m^3}\right]$
Specific heat capacity, $c_{p,air}$	1005.0	$\left[\frac{J}{kgK}\right]$
Thermal conductivity, k_{air}	0.0257	$\left[\frac{W}{mk}\right]$
Kinematic viscosity, ν_{air}	1.50E-5	$\left[\frac{m^2}{s}\right]$

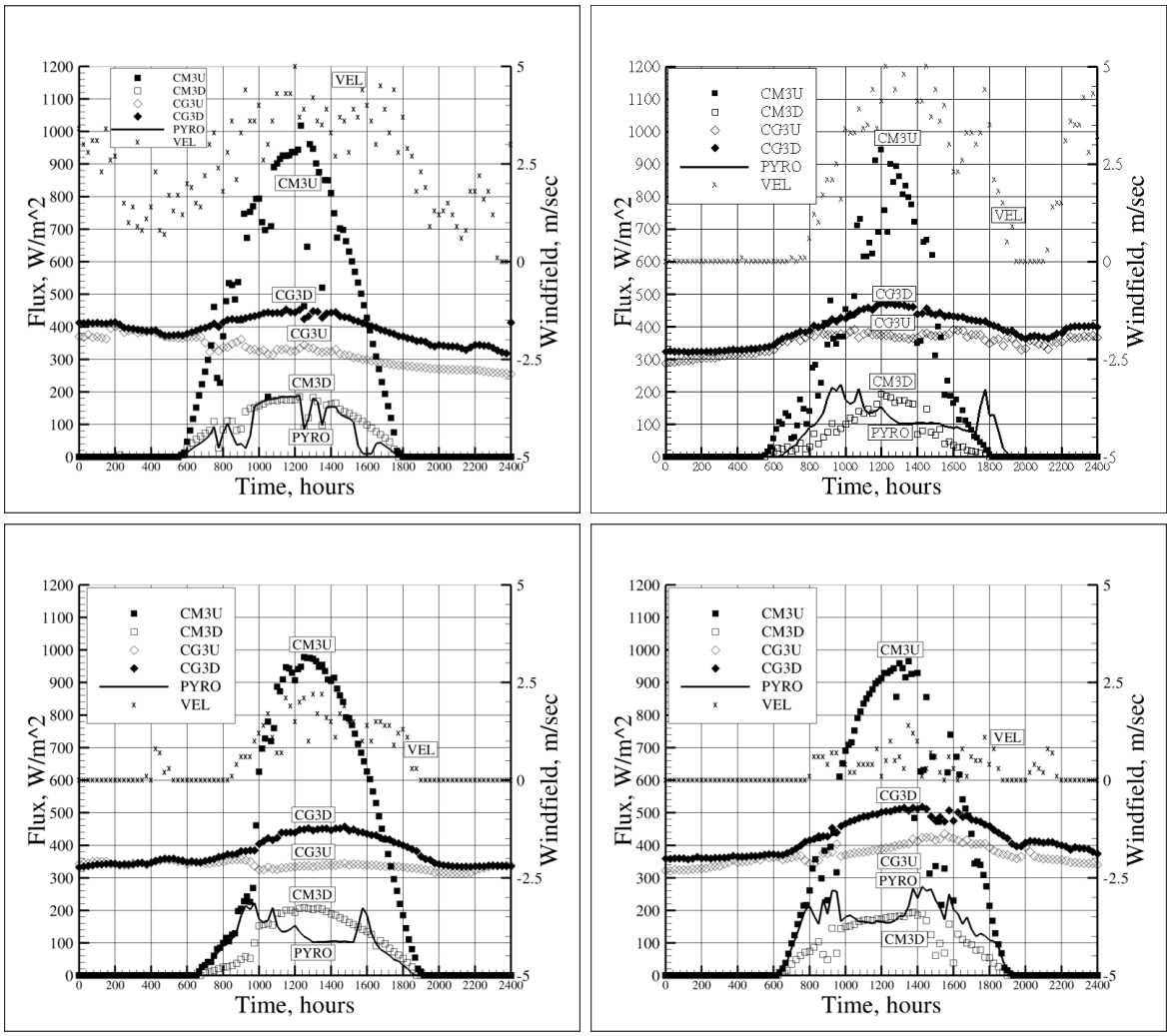

Figure A.1: View graph of meteorological data.

Commentary on fig. A.1, meterological data recorded for 24 hour period. Data set shown for 4 days, 04-03-2006 (top left), 04-06-2006 (top right), 04-12-2006 (bottom left), 04-18-2006 (bottom right).

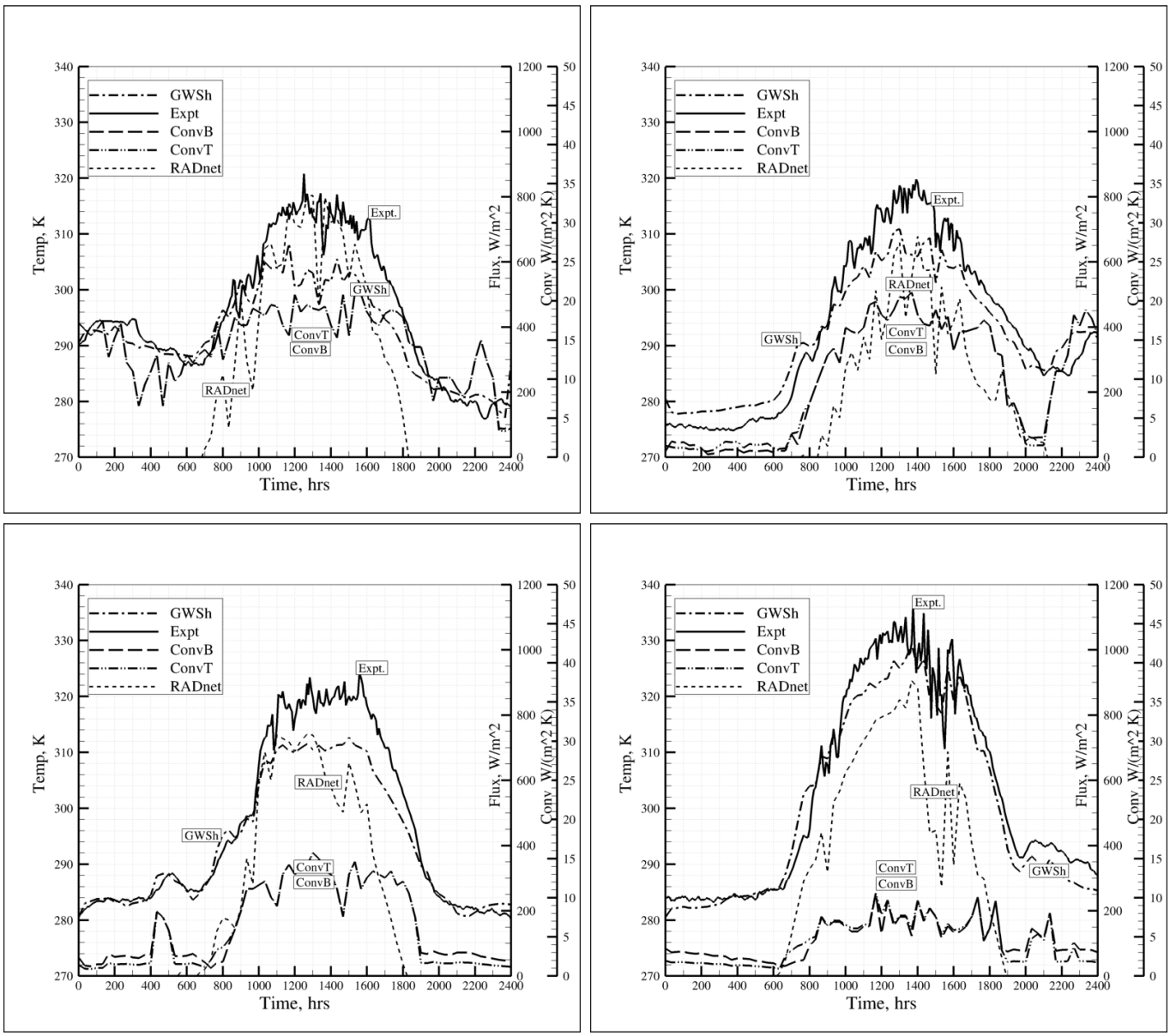

Figure A.2: Validation data for 1/8th plate, bottom forced and L=2x.

Commentary on Fig. A.2, Solution data aPSE comparison to EXPT for a 1/8 inch thickness plate, with L = 2x and applying a linear combination of forced and free convection on top and bottom side of the plate. Solution data, starting top left, going clockwise, 04-03-2006 (top left), 04-06-2006 (top right), 04-12-2006 (bottom left), 04-18-2006 (bottom right).

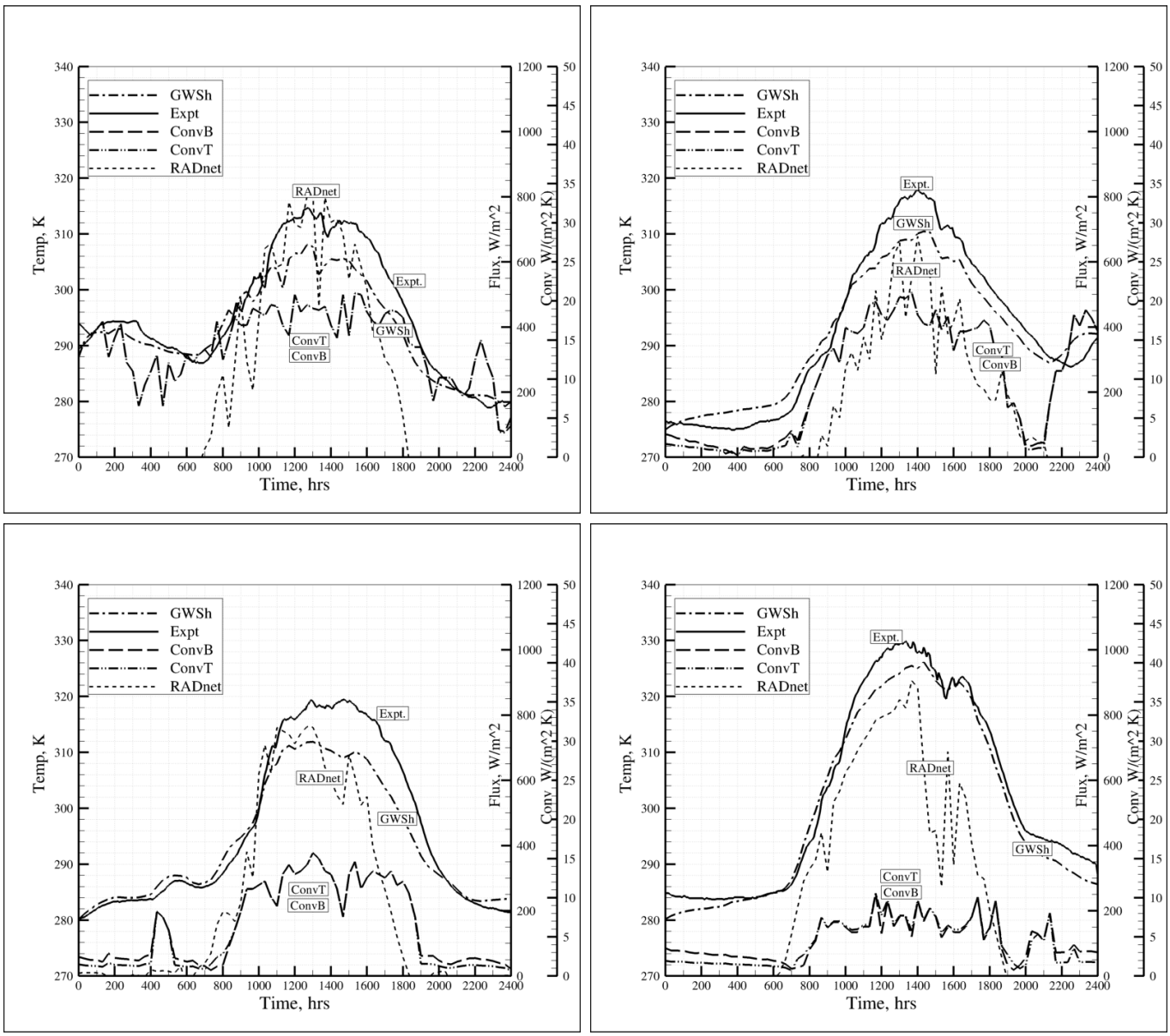

Figure A.3: Validation data for 1 inch plate, bottom forced, and L=2x.

Commentary on Fig. A.3, Solution data aPSE comparison to EXPT for a 1 inch thickness plate, similar settings as in Fig. A.2.

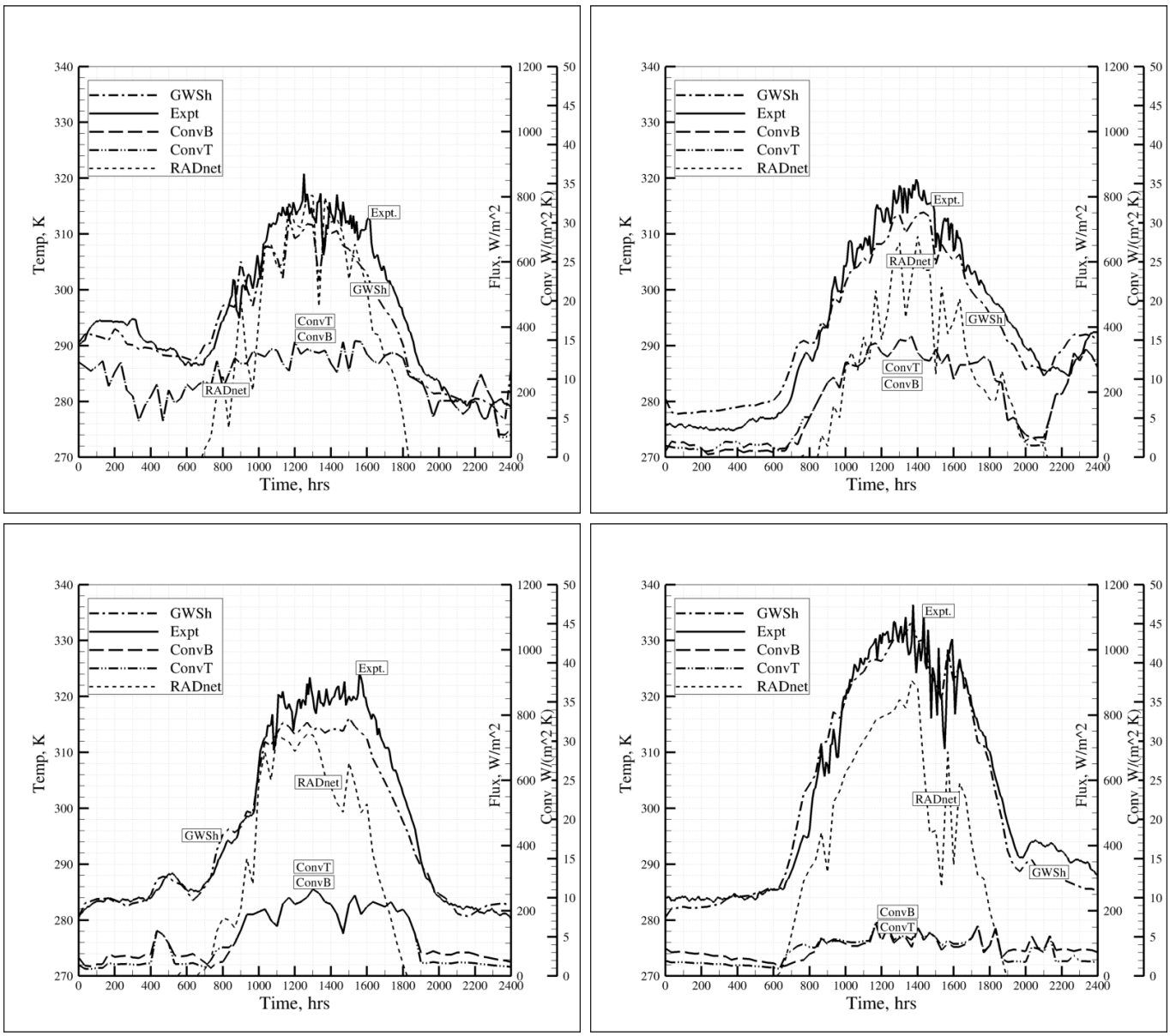

Figure A.4: Validation data for 1/8th plate, bottom forced, and L=1x.

Commentary on Fig. A.4, Solution data aPSE comparison to EXPT for a 1/8 inch thickness plate, with L = 1x and applying a linear combination of forced and free convection on top and bottom side of the plate. Solution data, starting top left, going clockwise, 04-03-2006 (top left), 04-06-2006 (top right), 04-12-2006 (bottom left), 04-18-2006 (bottom right). The convection mechanism is turned on for both top and bottom side of plate.

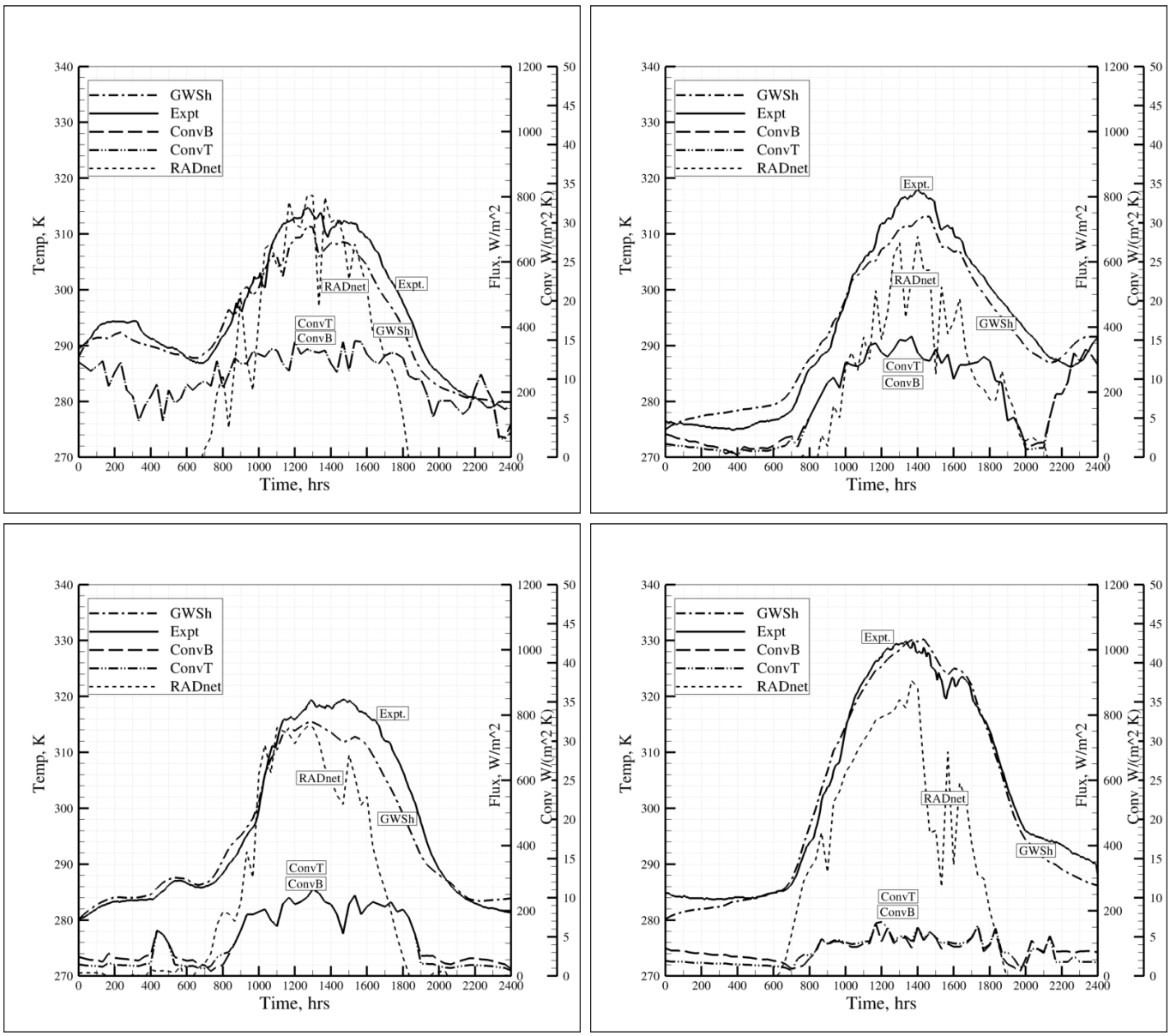

Figure A.5: Validation data for 1 inch plate, bottom forced, and L=1x.

Commentary on Fig. A.5, Solution data aPSE comparison to EXPT for a 1 inch thickness plate, with L = 1x and applying a linear combination of forced and free convection on top and bottom side of the plate. Solution data, starting top left, going clockwise, 04-03-2006 (top left), 04-06-2006 (top right), 04-12-2006 (bottom left), 04-18-2006 (bottom right). The convection mechanism is turned on for both top and bottom side of plate.

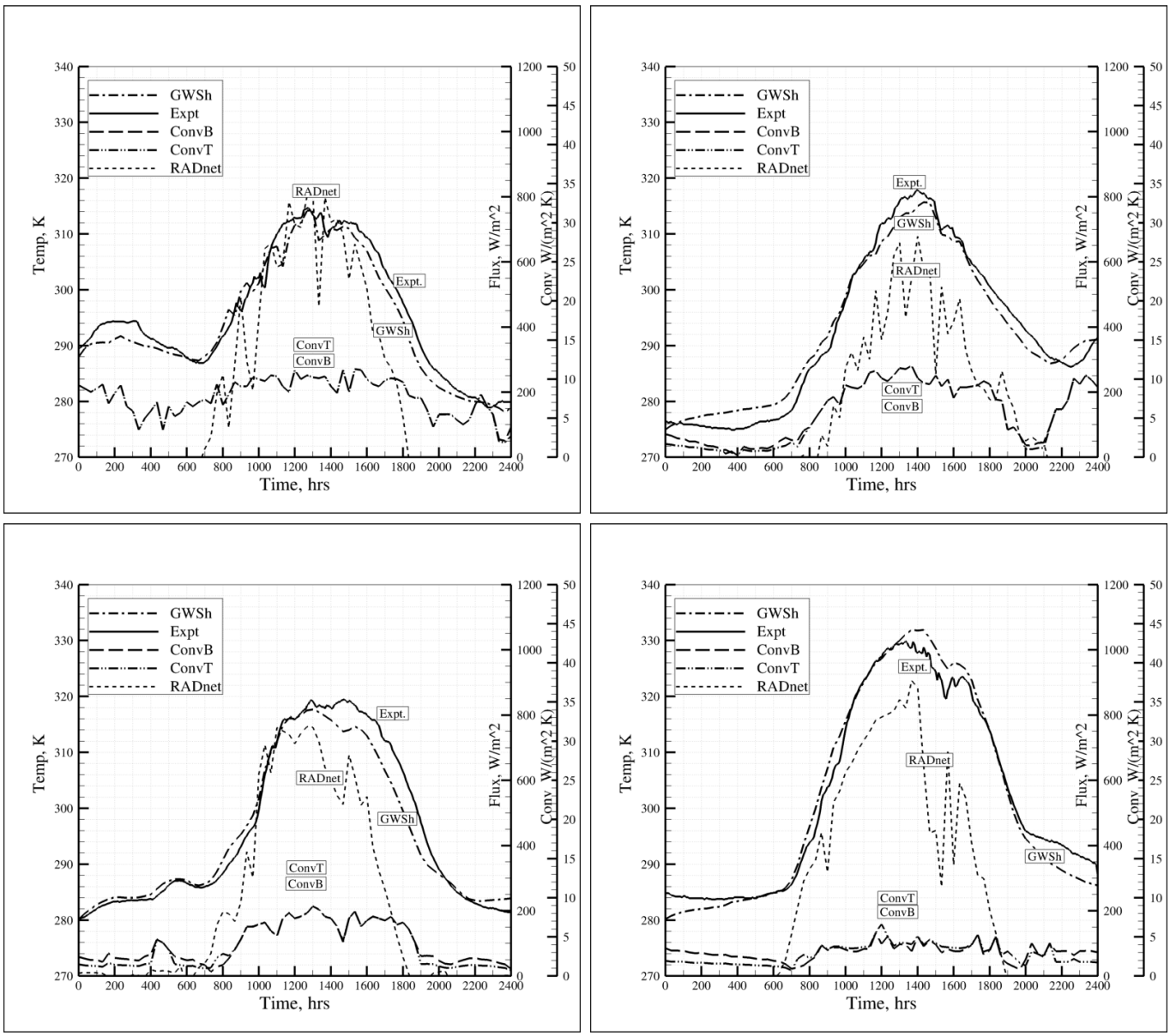

Figure A.6: Validation data for 1 inch plate, bottom forced, and L=0.6 and x=0.3.

Commentary on Fig. A.7, Solution data aPSE comparison to EXPT for a 1 inch thickness plate, similar settings as in Fig. A.2.

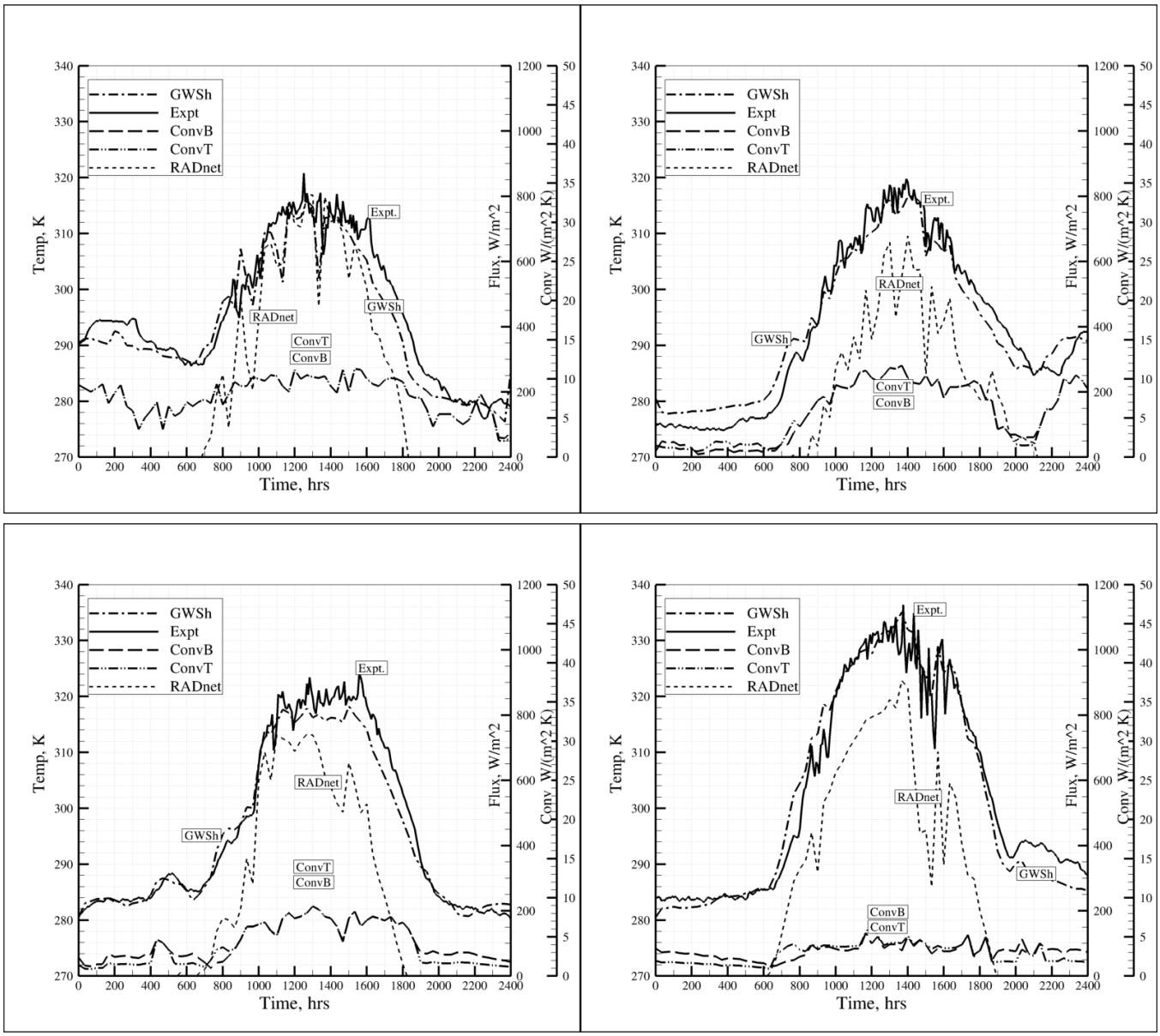

Figure A.7: Validation data for 1/8 inch plate, bottom forced, and L=0.6 and x=0.3.

Commentary on Fig. A.7, Solution data aPSE comparison to EXPT for a 1/8 inch thickness plate, similar settings as in Fig. A.2.

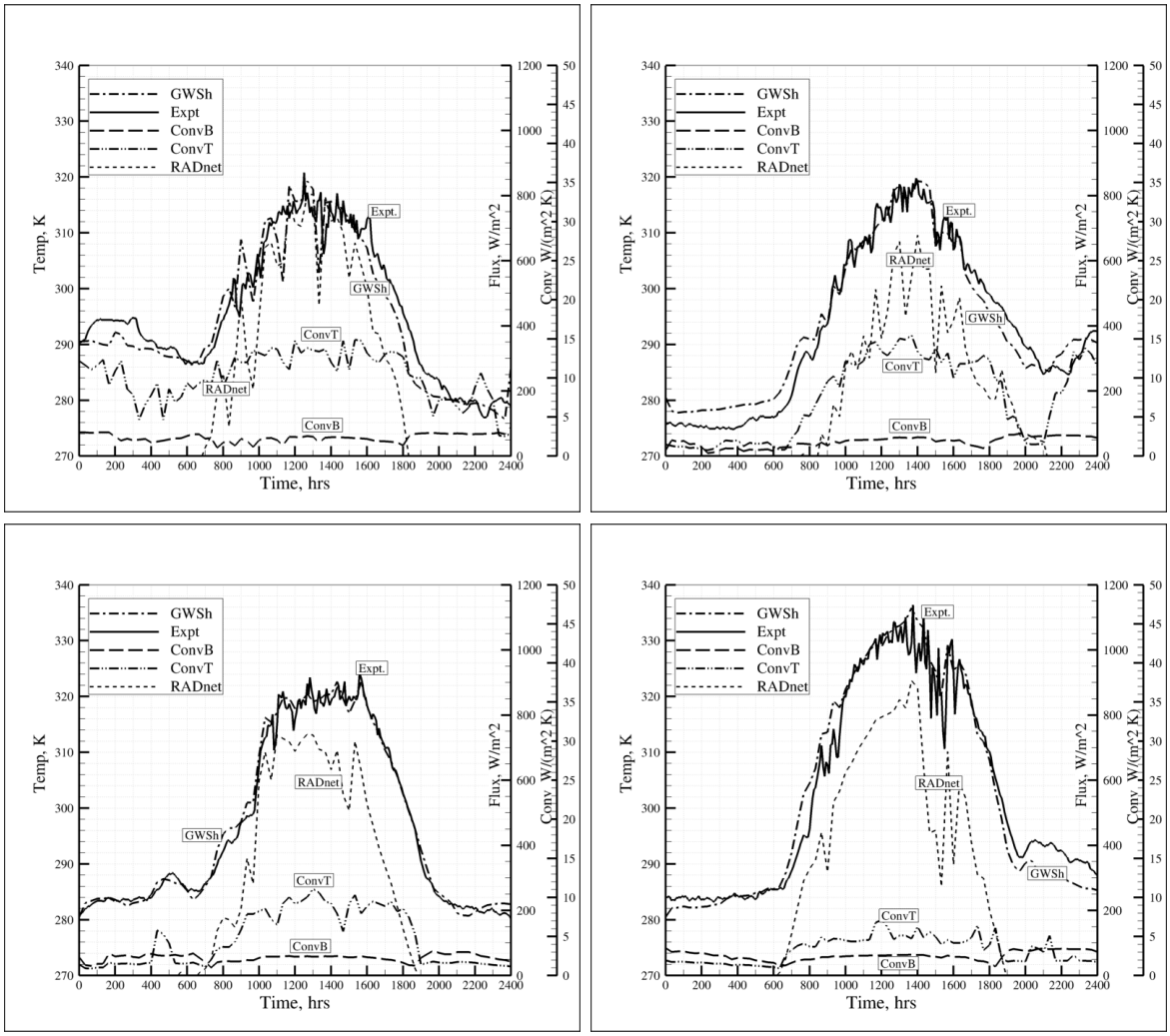

Figure A.8: Validation data for 1/8 inch plate, no-bottom-forced, and L=1x.

Commentary on Fig. A.8, Solution data aPSE comparison to EXPT for a 1/8 inch thickness plate, with L = 1x and applying a free convection on bottom side of the plate. Solution data, starting top left, going clockwise, 04-03-2006 (top left), 04-06-2006 (top right), 04-12-2006 (bottom left), 04-18-2006 (bottom right). The convection mechanism is turned on for both top and bottom side of plate.

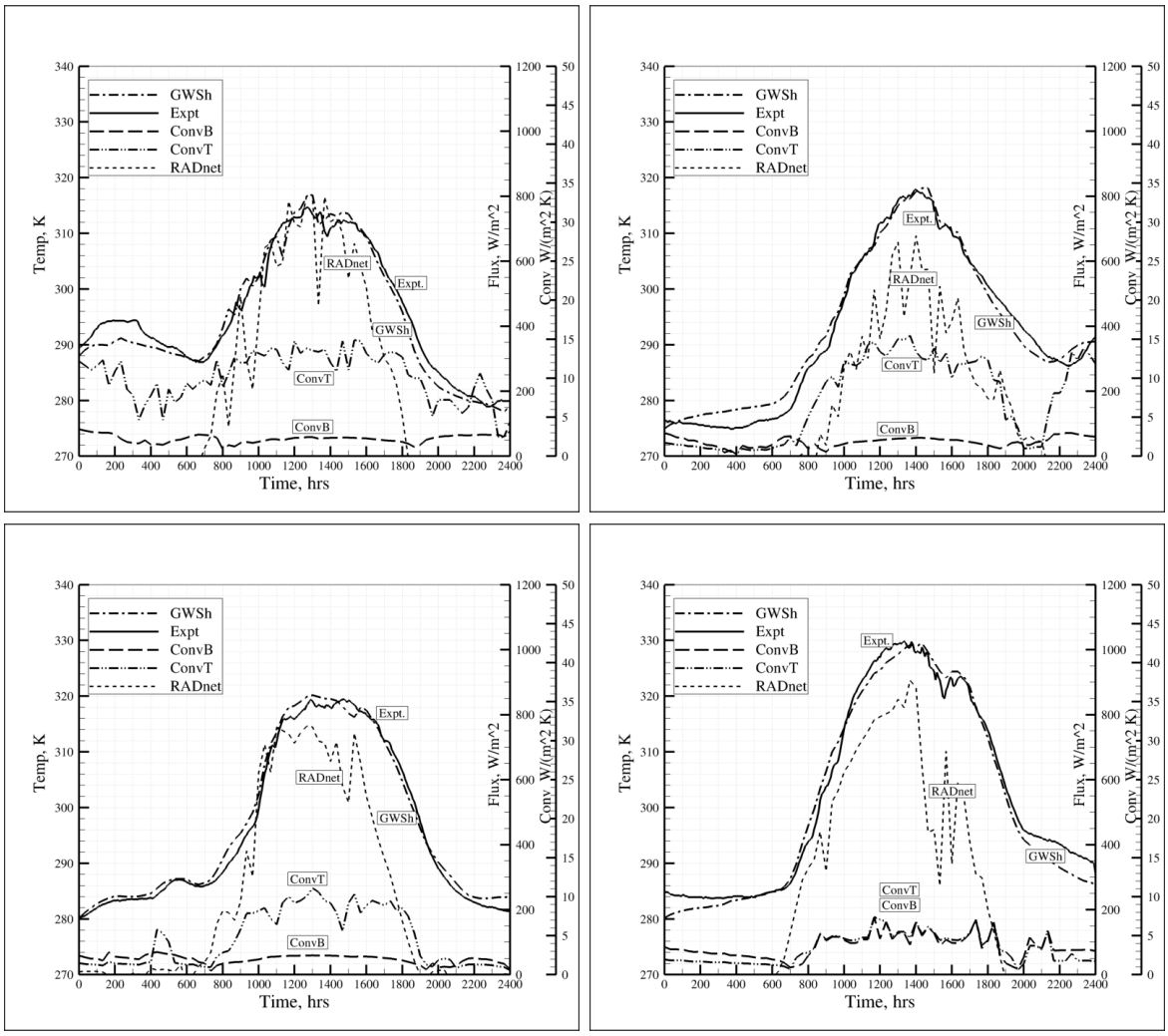

Figure A.9: Validation data for 1 inch plate, no-bottom forced, and L=1x.

Commentary on Fig. A.9, solution data aPSE comparison to EXPT for a 1 inch thickness plate, with L = 1x and applying a free convection on both side of the plate. Solution data, starting top left, going clockwise, 04-03-2006 (top left), 04-06-2006 (top right), 04-12-2006 (bottom left), 04-18-2006 (bottom right). The convection mechanism is turned on for both top and bottom side of plate.

Vita

Elton Lewis Freeman was born in Rome, Georgia, on September 7^{th}, 1974. He graduated from Pepperell High School in May of 1994. He then graduated from State University of West Georgia with bachelor of Science (Bs) in Physics in the Spring of 2004. In the year of his graduation, Elton was awarded the Who's Who award, and he gave many talks at the Georgia Academy of Science. His talks titled "RC Low Pass Filter", Georgia Academy of Sciences on campus of Rhineheart College, 2003. He gave another talk titled "Alpha Particle Tunneling", with the Georgia Academy of Sciences at Berry College, 2004.

He was highly interested in Nuclear Physics, so he was accepted to the Physics Department as a graduate teaching assistant in the fall of 2005. He won the "Robert E. Lide" award for outstanding achievement in laboratory service. In Summer of 2008, Elton finished his masters degree in physics with speciality in experimental nuclear physics and with a minor in nuclear engineering. During that time he was also inducted into the Sigma Pi Sigma, Physics Honory Society. Elton then became a science and math teacher at the Tennessee Governor's Academy of Math and Science from 2008 to 2010. He taught pre-calculus, calculus, ordinary differential equations, and physics labs to outstanding high school students of the State of Tennessee. Later in that same year, Elton decided to take engineering courses at the University of Tennessee. This decision was in part due to his adviser, Dr. A.J.Baker, who thought he had real potential in the engineering science field by having a background

in physics. Elton applied himself to the Mechanical Aerospace and Biomedical Engineering Department at University of Tennessee as a Graduate Research Assistant for 3 years until his graduation with another Masters degree in the Fall of 2012 in Engineering Science. While working on his degree, Elton also gave a talk titled "Validation of an Unsteady 2.5D Thermal Convection-Radiation Finite Element Algorithm" at International Test and Evaluation Association (I.T.E.A), Annapolis Maryland, July 2010. In that year, Elton was involved in a group representation titled "A Scalable Software Framework for Thermal Radiation Simulation" that won first prize in XSEDE's "best graduate poster award" in the summer of that same year.

Eltons interest in the thermal sciences has led him to persuit the combustion sciences with Dr. Sakaran Rammanan. Elton enjoys using the worlds most power super computer, TITAN, to model and simulation the combustion mechanisms using new technology of graphics programming units.